DOT/FAA/TC-19/41, P4

Federal Aviation Administration
William J. Hughes Technical Center
Aviation Research Division
Atlantic City International Airport
New Jersey 08405

Aluminum 2024-T351 Input Parameters for *MAT_224 in LS-DYNA

Part 4: Ballistic Impact Simulations of a Titanium 6Al-4V Generic Fan Blade Fragment on an Aluminum 2024 Panel Using *MAT_224 in LS-DYNA

September 2021

Final report

U.S. Department of Transportation
Federal Aviation Administration

NOTICE

This document is disseminated under the sponsorship of the U.S. Department of Transportation in the interest of information exchange. The U.S. Government assumes no liability for the contents or use thereof. The U.S. Government does not endorse products or manufacturers. Trade or manufacturers' names appear herein solely because they are considered essential to the objective of this report. The findings and conclusions in this report are those of the author(s) and do not necessarily represent the views of the funding agency. This document does not constitute FAA policy. Consult the FAA sponsoring organization listed on the Technical Documentation page as to its use.

This report is available at the Federal Aviation Administration William J. Hughes Technical Center's Full-Text Technical Reports page: actlibrary.tc.faa.gov in Adobe Acrobat portable document format (PDF).

Form DOT F 1700.7 (8-72) Reproduction of completed page authorized

1. Report No.	2. Government Accession No.	3. Recipient's Catalog No.
DOT/FAA/TC-19/41, P4		

4. Title and Subtitle	5. Report Date
Aluminum 2024-T351 Input Parameters for *MAT_224 in LS-DYNA Part4: Ballistic Impact Simulations of a Titanium 6Al-4V Generic Fan Blade Fragment on an Aluminum 2024 Panel Using *MAT_224 in LS-DYNA	September 2021
	6. Performing Organization Code

7. Author(s)	8. Performing Organization Report No.
Chung-Kyu Park[1], Kelly Carney[1], Paul Du Bois[1], Cing-Dao Kan[1], and Daniel Cordasco[2]	

9. Performing Organization Name and Address	10. Work Unit No. (TRAIS)
[1] George Mason University, Center for Collision Safety and Analysis 4087 University Drive, Fairfax, VA 22030 USA [2] Federal Aviation Administration, William J. Hughes Technical Center Atlantic City International Airport, NJ 08405	11. Contract or Grant No. 692M151840003

12. Sponsoring Agency Name and Address	13. Type of Report and Period Covered
U.S. Department of Transportation Federal Aviation Administration Air Traffic Organization Operations Planning Office of Aviation Research and Development Washington, DC 20591	Final Report
	14. Sponsoring Agency Code AIR-6A1

15. Supplementary Notes

The Federal Aviation Administration William J. Hughes Technical Center Aviation Research Division Technical Monitor was Daniel Cordasco.

16. Abstract

As a part of the FAA's Aircraft Catastrophic Failure Prevention Program, advanced material models have been developed to improve the numerical modeling of turbine engine blade-out events. In this effort, NASA conducted four ballistic impact tests on large flat Aluminum 2024 panels with a blade-shaped Titanium 6Al-4V projectile to provide experimental data to evaluate the numerical material models. These tests were designed to represent the release of a metallic turbine engine fan blade. When the tip of a released metallic fan blade makes contact with the engine case the tip skates as the blade bends and rotates, causing the heavy blade root to impact, and potentially penetrate, the engine case.

The ballistic impact tests were simulated using advanced Aluminum 2024 and Titanium 6Al-4V material model parameters previously developed in this research in conjunction with LS-DYNA's *MAT_224 constitutive material model. The simulations validate these material models under more realistic turbine engine blade release event conditions and identify possible challenges for such a ballistic impact simulation with a blade-shaped projectile that slides, bends, plastically deforms, and rotates in three dimensions.

Half-symmetric and full FE models were created using 0.01-inch elements. These models contained over 41 million and 82 million solid elements, respectively. Overall, the ballistic impact simulations showed results similar to the tests in terms of the panel deformation and blade behavior, and could predict the panel perforation. However, generic limitations of the simulation, such as use of element erosion, resulted in the absence of wear debris, which necessitated adjusting contact friction coefficients to correlate with test results. This accommodation would be anticipated to affect the wear mark size, crack propagation, and petal size in the simulations.

17. Key Words	18. Distribution Statement
ballistic impact simulation, fan blade off, turbine engine containment, Aluminum 2024, Titanium 6AL-4V, *MAT_224, LS-DYNA	This document is available to the U.S. public through the National Technical Information Service (NTIS), Springfield, Virginia 22161. This document is also available from the Federal Aviation Administration William J. Hughes Technical Center at actlibrary.tc.faa.gov.

19. Security Classif. (of this report)	20. Security Classif. (of this page)	21. No. of Pages	22. Price
Unclassified	Unclassified		

Acknowledgements

The authors would like to express our gratitude to Dr. Mike Pereira, Mr. Duane Revilock, and Mr. Charles Ruggeri, Aerospace Engineers at NASA Glenn Research Center, for sharing their insight and expertise along with the test data, photos and videos generated during the tests. Their support greatly assisted with this research.

The authors are also grateful to Mr. William Emmerling (retired) at FAA William J. Hughes Technical Center for his constant support and advice on this research, and Dr. Gilbert Queitzsch (retired) at FAA for his helpful discussion and feedback for this research.

This research was conducted under FAA cooperative agreement 692M151840003 and sponsored by the Aircraft Catastrophic Failure Prevention Program (ACFPP).

Contents

Figures

Tables

Acronyms

Acronym	Definition
ACFPP	Aircraft Catastrophic Failure Prevention Program
DIC	Digital Image Correlation
DOF	Degree of Freedom
FAA	Federal Aviation Administration
FE	Finite Element
GMU	George Mason University
GRC	Glenn Research Center
GWU	George Washington University
NASA	National Aeronautics and Space Administration
NGFBF	NASA Generic Fan Blade Fragment
OSU	Ohio State University

Executive summary

As a part of the FAA's Aircraft Catastrophic Failure Prevention Program, advanced material models have been developed to improve the numerical modeling of turbine engine blade-out containment tests required for certification of aircraft engines.

In this effort, NASA conducted four ballistic impact tests on large flat Aluminum 2024 panels with a blade-shaped Titanium 6Al-4V projectile to provide experimental data to evaluate the numerical material model. These tests were designed to represent a realistic turbine engine fan-blade release event. When the tip of a released metallic fan blade makes contact with the engine case, it skates as the tip bends and usually fractures. Skating slows the tip causing the blade to rotate, driving the heavy blade root to impact the engine case. If the blade penetrates the case, it will normally be the high energy root impact that initiates the case failure and not the lower energy tip impact and skating.

The ballistic impact tests were simulated using advanced Aluminum 2024 and Titanium 6Al-4V material models previously developed in this research in conjunction with LS-DYNA's *MAT_224 constitutive material model. The simulations validate these material models under simulated turbine engine blade release event conditions. The research also identifies possible challenges for such a ballistic impact simulation with a blade-shaped projectile that slides, bends (plastically deforms), and may fracture, and rotates as it moves in three dimensions.

The half-symmetric and full Finite Element (FE) models were created with 0.01-inch elements resulting in models with over 41 million and 82 million solid elements, respectively. Overall, the ballistic impact simulations showed results similar to the tests in terms of panel deformation and blade behavior and could predict the panel perforation. However, generic limitations of the simulation, such as use of element erosion, resulted in the absence of the wear debris, which necessitated adjusting contact friction coefficients to correlate with test results. This accommodation would be anticipated to affect the wear mark size, crack propagation, and petal size in the simulations.

1 Introduction

A team consisting of George Mason University (GMU), Ohio State University (OSU), George Washington University (GWU), the National Aeronautics and Space Administration (NASA) - Glenn Research Center (GRC), and the Federal Aviation Administration (FAA) - Aircraft Catastrophic Failure Prevention Program (ACFPP) collaborated to develop a new material model in LS-DYNA for metallic materials. The research was directed towards improving the numerical modeling of turbine engine blade-out containment tests required for certification of aircraft engines (Emmerling, Altobelli, Carney, & Pereira, 2014; Buyuk, 2014). In this effort, the LS-DYNA constitutive material model *MAT_TABULATED_ JOHNSON_COOK, or simply *MAT_224, was applied. *MAT_224 is a general elasto-visco-plastic material model that utilizes a tabulated approach to incorporate arbitrary stress versus strain curves to define material plasticity, including arbitrary strain rate and temperature dependency. The element erosion criterion is the plastic failure strain, which can be defined as a function of the state of stress, strain rate, temperature, and element size.

The updated *MAT_224 input parameters (Version 2.2) for Aluminum 2024-T351 alloy plates (Park, Carney, Du Bois, Cordasco, & Kan, 2020) were developed based on tabulated data from several material tests performed by OSU (Seidt, 2014), and was released recently (LS-DYNA Aerospace Working Group, 2021). It has been validated intensively with three series of ballistic impact tests: (1) ballistic impact tests of a sphere projectile to square Aluminum 2024 plates with various thicknesses (Park, Carney, Du Bois, Cordasco, & Kan, 2020) (Kelley & Johnson, 2006), (2) ballistic impact tests of a cylinder projectile to circular Aluminum 2024 plates with various thicknesses (Park, Carney, Du Bois, Cordasco, & Kan, 2020) (Pereira, Revilock, Lerch, & Ruggeri, 2013), and (3) ballistic impact tests of 1/8-inch thick Aluminum 2024 plates with rectangular projectiles, having varying oblique incidence and attitude angles (Pereira, Revilock, Lerch, & Ruggeri, 2013) (Park, et al., 2020). Overall, the ballistic impact simulations using the updated Aluminum 2024 *MAT_224 material model show good correlations to the lab tests for a broad range of test conditions. In addition, the *MAT_224 input parameters for a Titanium 6Al-4V alloy Version 1.3, (LS-DYNA Aerospace Working Group, 2021) projectile were also developed using a series of material tests conducted by OSU (Haight, Wang, Du Bois, Carney, & Kan, 2016) (Hammer, 2014). It was validated with dynamic punch tests (Haight, Wang, Du Bois, Carney, & Kan, 2016) (Hammer, 2014) and ballistic tests of cylinder projectiles impacting circular 1/2-inch thick Titanium 6Al-4V plates (Pereira, Revilock, Lerch, & Ruggeri, 2013) (Haight, Wang, Du Bois, Carney, & Kan, 2016).

Four ballistic impact tests on large flat Aluminum 2024 panels with a blade-shaped Titanium 6Al-4V projectile were conducted by the NASA Glenn Research Center to provide experimental data to evaluate the numerical material model (Pereira, Revilock, Lerch, & Ruggeri, 2013). These tests were designed to represent key aspects of a real turbine engine fan-blade release event, where a released fan blade tip makes contact with the engine case, bends, may fracture, and then rotates to cause the heavy blade root to impact (and potentially penetrate) the engine case. In all the tests, the projectiles were contained, but the panels were perforated in three tests. The critical velocity of the panel perforation was estimated based on the test data.

In this research, these ballistic impact tests were simulated using advanced Aluminum and Titanium material models using *MAT_224 in LS-DYNA. This effort had two objectives: (1) to further validate those material models under more realistic turbine engine blade release event conditions and (2) to identify possible challenges for similar ballistic impact simulations. In the ballistic impact tests, the blade-shaped projectile rotates and moves in three dimensions, has prolonged sliding contact with the target plate, and exhibits significant plastic deformation. An accurate simulation must exhibit all of these characteristics. Both a half-symmetric simulation model with about 41 million solid elements, and full simulation model with about 82 million solid elements were developed. Comparisons between the tests and the simulations showed both promising results and limitations. These limitations will be addressed.

2 NASA blade impact tests

NASA conducted four ballistic impact tests on large flat Aluminum 2024 panels with a simulated blade-shape Titanium 6Al-4V projectile to provide experimental data to evaluate the numerical material model (Pereira, Revilock, Lerch, & Ruggeri, 2013). These tests were designed to simulate characteristics of a turbine engine blade release event where a released blade tip makes contact with the engine case, skates (slides), bends, and then rotates to cause the heavier blade root to impact and potentially penetrate the engine case. This section briefly summarizes the NASA blade impact tests.

2.1 Test setup

The projectile developed for this study, called the NASA Generic Fan Blade Fragment (NGFBF), was designed to include some of the features of a real fan blade, such as a thin tip and heavy root, while being relatively simple to manufacture and model. It was made from Titanium 6Al-4V and had a nominal mass of 340 grams. Its dimensions are shown in Figure 1.

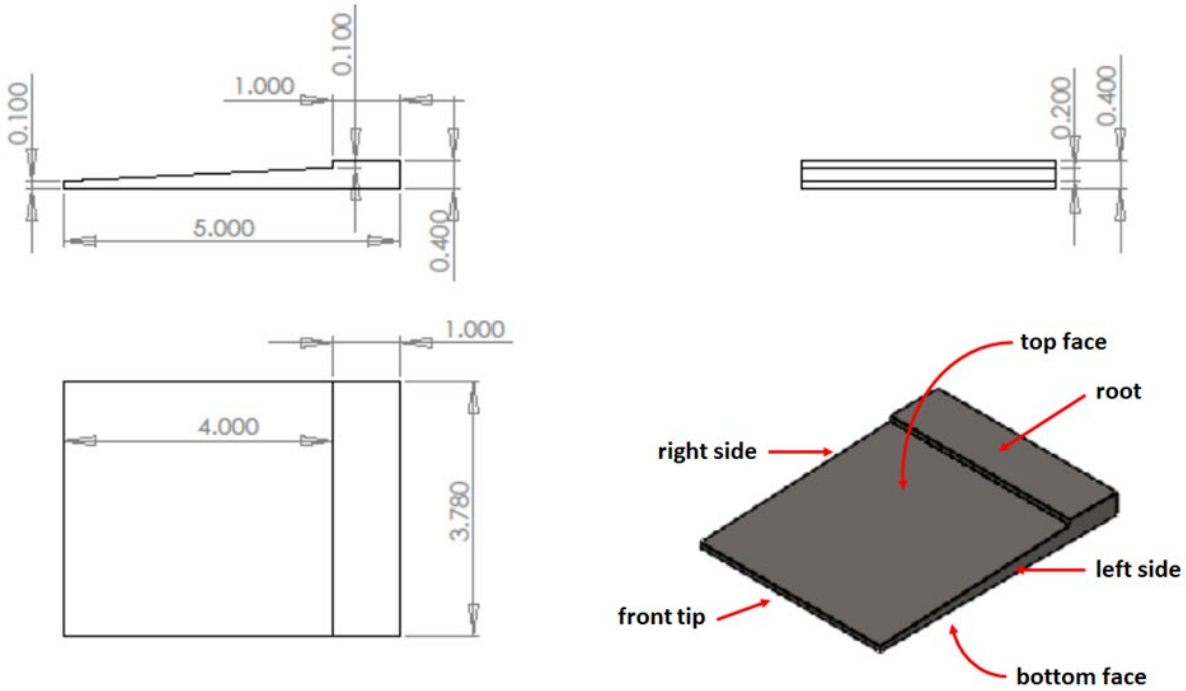

Figure 1. NGFBF projectile (dimensions in inches) (Pereira, Revilock, Lerch, & Ruggeri, 2013)

The test panels were 24.0 inches by 24.0 inches with a nominal thickness of 0.25 inches and were made from Aluminum 2024-T351. The panels were held at a 45° angle in a square fixture with a 20.0-inch by 20.0-inch aperture, as shown in Figure 2. The nominal impact obliquity angle defined by the angle between the projectile flight direction and panel normal direction was 45° in the ballistic impact tests. The panels were through-bolted with 24 0.5-inch bolts equally spaced around the sides, 1.0 inch inside from the edges.

Figure 2. Schematic of the test setup (Pereira, Revilock, Lerch, & Ruggeri, 2013)

The blade projectile was initially positioned with a 45° angle in a gun barrel, which makes an initial 90° angle between the panel and the blade projectile, as shown in Figure 2. However, actual impact angles between the panel and the blade projectile at the impact moment in the tests were much less (45.1° - 61.3°) because the blade projectiles rotated while they were flying from the gun barrel to the impact point on the panel.

Full field displacement data on the back side of the impacted panels were obtained by using a pair of calibrated high-speed cameras and a Digital Image Correlation (DIC) system to measure the deformation of the panels. In addition, a second pair of calibrated cameras on the impact side of the panel were used to track the position of the projectile. Photogrammetry software used the recorded positions of individual points on the projectile to do this tracking. The impact velocity and orientation of the projectile were computed from these data.

Figure 3 shows the two coordinate systems: the global fixed coordinate system and the blade local moving coordinate system. The origin of the global coordinate system is fixed at the center of the impact front face of the test panel. The **X**-axis of the global coordinate system is parallel to the flying direction of the projectile, as indicated by the yellow dashed line, and the **Z**-axis of the global coordinate system points vertically downward. The origin of the blade local coordinate system is located at a point on the left lower root of the blade, 0.5 inch from the lower root edge and 0.5 inch from the left side edge, as shown in Figure 3. The $\mathbf{x_b}$-axis and $\mathbf{y_b}$-axis of the blade

local coordinate system point toward the left tip corner and the right root corner of the blade, parallel to the left side edge and the root edge of the blade, respectively. The blade local coordinate system is moving and rotating with the blade projectile.

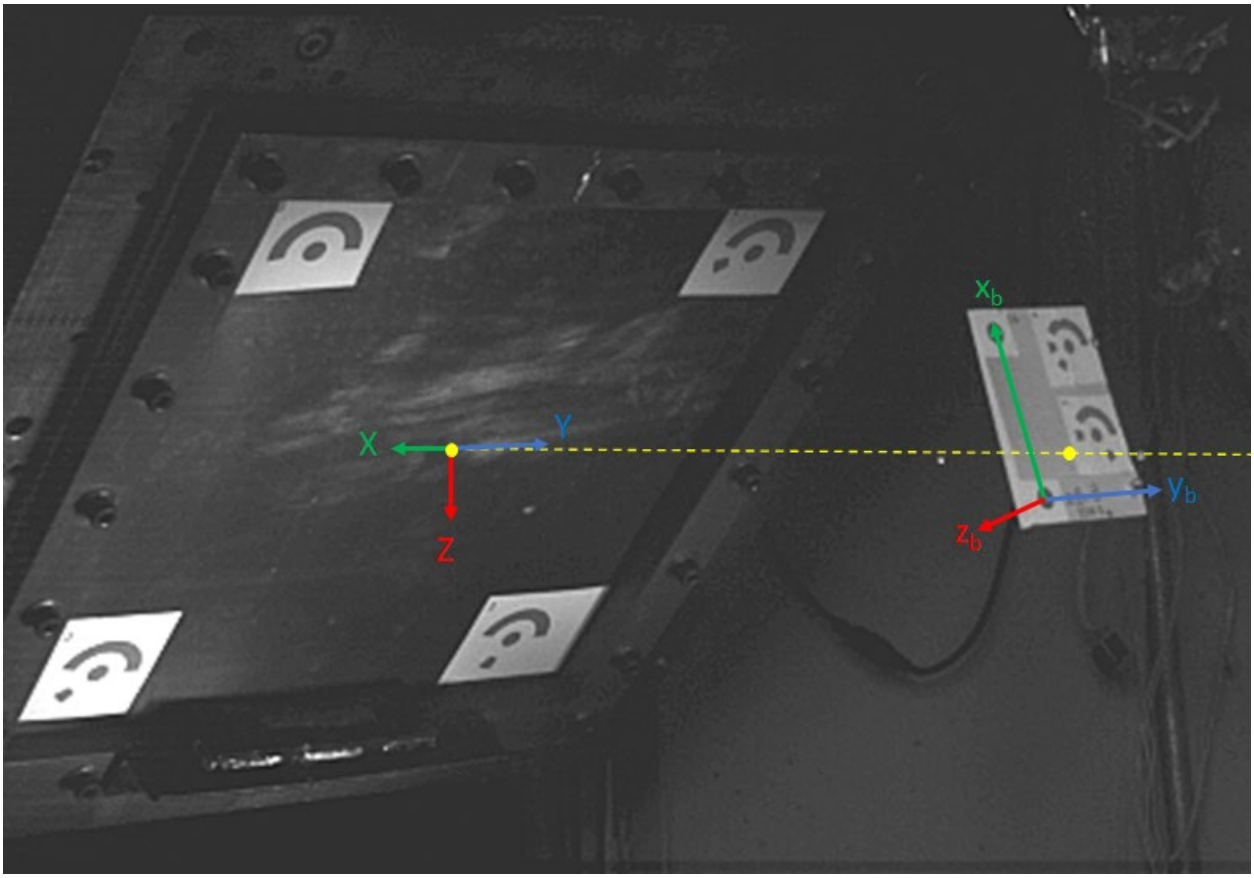

Figure 3. Two coordinate systems on the still image from high-speed movie of the impact test

2.2 Test results

A total of four ballistic impact tests (LG908, LG909, LG910, and LG911) were conducted with the test setup described above. The four tests had the same conditions, except for the intentionally differing initial impact velocities, and the unavoidably differing blade orientations. Figure 4 shows several impact stages of the LG909 test. First, in Figure 4(a), the left, corner of the blade projectile tip made the first contact on the surface of the panel after the blade projectile was propelled from the gun barrel. Then, the blade tip started bending as the blade tip skidded on the panel. This slowed the blade tip causing the blade to rotate driving the root into the plate, as shown in Figure 4(b)-4(c). When the blade root impacted the plate and continued to slide, the root bottom edge gouged the panel surface deeply, removing many small pieces of debris from the panel surface, as indicated by the ejected debris highlighted in the yellow oval in Figure 4(d). Finally, the blade root perforated the panel, as shown in Figure 4(e). Figure 4(f) shows the perforation on the post-tested panel. The progression of damage during the event can be observed in Figure 4, which progresses from initial deep scratches to perforation, to crack propagation, and to petal development. This impact progression occurred similarly in tests LG910 and LG911. Test LG908 was different because the panel was not perforated indicating the plate damage did not progress beyond surface damage. In all tests, the projectile was contained and rebounded from the panel.

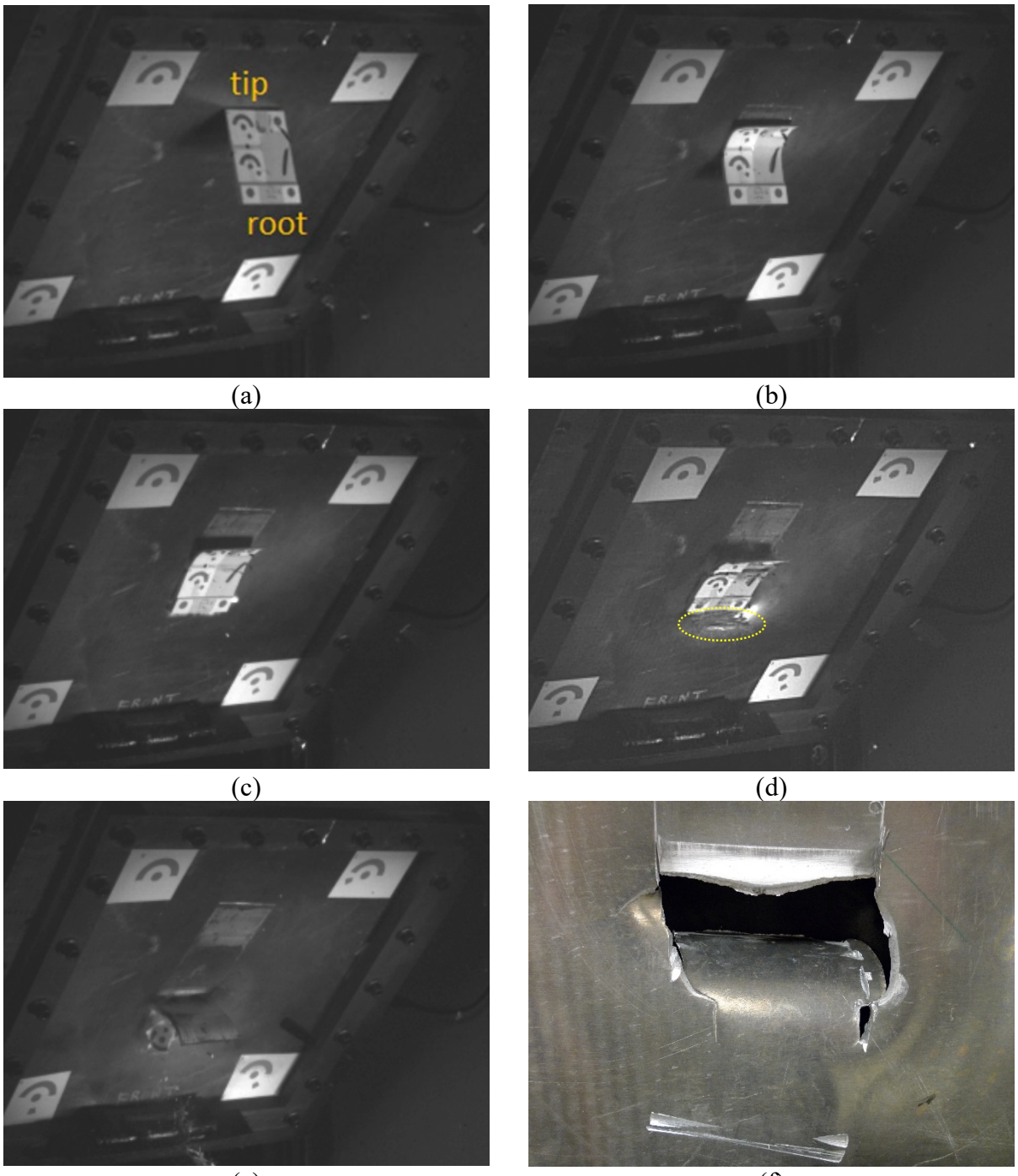

Figure 4. Snapshots of LG909: (a) blade tip edge impact, (b) blade tip bending, (c) blade root bottom face impact, (d) blade root edge scratching, (e) blade root perforating, and (f) post-test perforation on the panel

Figure 5 shows the scraping by the blade root edge more clearly, where it made a wide and deep scrape on the panel surface in the LG908 test. Many small pieces of debris were observed chipping out and ejected ahead of the root, as indicated by the yellow oval in Figure 5(a).

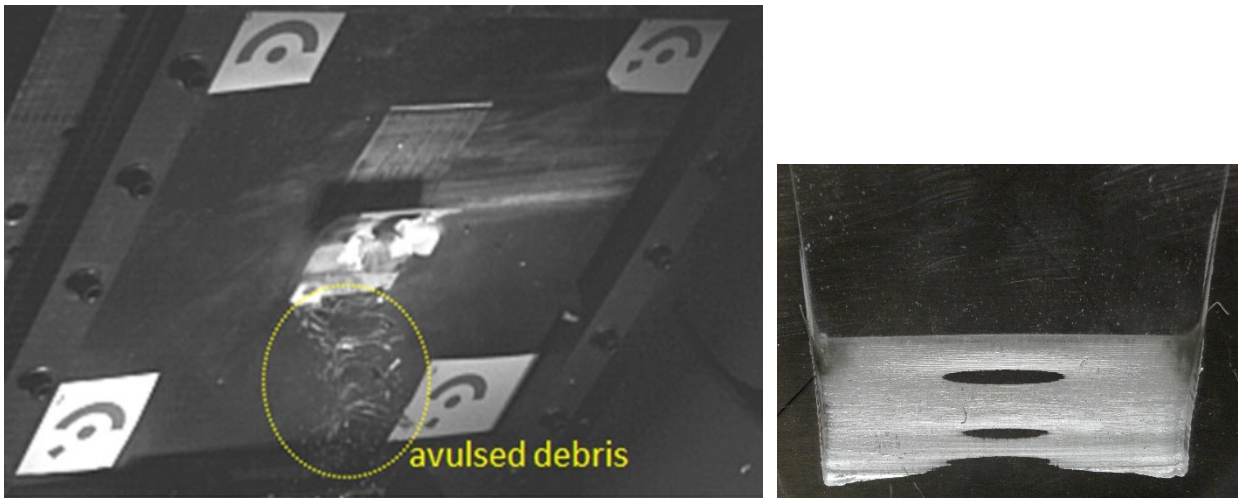

(a) (b)

Figure 5. Snapshots of LG908: (a) blade root edge scratching; and (b) damage on the panel

Table 1 summarizes the measured linear velocities of the blade projectile at the moment of initial tip impact. Specifically, the linear velocities of the blade projectile were measured at the origin of the local blade coordinate system (see Figure 3) in the global coordinate system. The angular positions and angular velocities of the blade projectile at the impact moment are summarized in Table 2. The angular orientation and angular velocity are given as a set of Euler angles with respect to the blade local moving coordinate system. The Euler angles are defined as an $\mathbf{x_b}$-$\mathbf{y_b}$-$\mathbf{z_b}$ rotation sequence: roll in the $\mathbf{x_b}$-axis, pitch in the $\mathbf{y_b}$-axis, and yaw in the $\mathbf{z_b}$-axis. The desired orientation (attitude angles) of the projectile at impact was (0°, 45°, 0°). However, actual orientations of the projectile were somewhat different due to the difficulty of precisely controlling orientation in the impact tests. This difficulty is due to unavoidable blade rotations. It should be noted that the values in Table 1 and Table 2 are different from those in the report (Pereira, Revilock, Lerch, & Ruggeri, 2013) because they were re-computed from the test data, and updated here, to correct faults that were found later in the original computation.

Table 1. Measured linear velocities of the blade projectile at impact moment

Test number	**Linear velocity**			**Comments**
	X-vel. (ft/s)	**Y**-vel. (ft/s)	**Z**-vel. (ft/s)	
LG908	712.8	7.9	-52.2	Contained
LG909	813.2	11.5	-10.7	Contained, Perforated
LG910	760.7	7.8	-11.0	Contained, Perforated
LG911	723.3	2.3	-7.4	Contained, Perforated

Table 2. Measured angular orientations and velocities of blade projectile at impact moment

Test number	**Angular orientation**			**Angular velocity**		
	Roll (deg.)	Pitch (deg.)	Yaw (deg.)	Roll vel. (deg/s)	Pitch vel. (deg/s)	Yaw vel. (deg/s)
LG908	-2.0	89.9	-1.5	-626.4	8255.4	71.8
LG909	2.6	73.7	0.1	-2.5	7664.4	-55.2
LG910	-0.7	79.1	2.3	193.0	7202.3	-669.0
LG911	8.2	82.8	1.1	343.5	7888.1	1007.3

The containment and perforation results for the panels in each test are identified in Table 2. While in all tests the projectiles were contained (i.e. they did not fully penetrate the panel), perforation of the panels occurred in the three higher velocity tests (LG909, LG910 and LG911). There was no panel perforation in the lowest velocity test, LG908. The deformed shapes of the post-tested panels are shown in Figure 6 through Figure 9. It can be seen that the majority of the damage and failure initiation occurred when the heavier root section of the blade impacted the panel. This is consistent with what occurs in an actual turbine engine fan blade out incident.

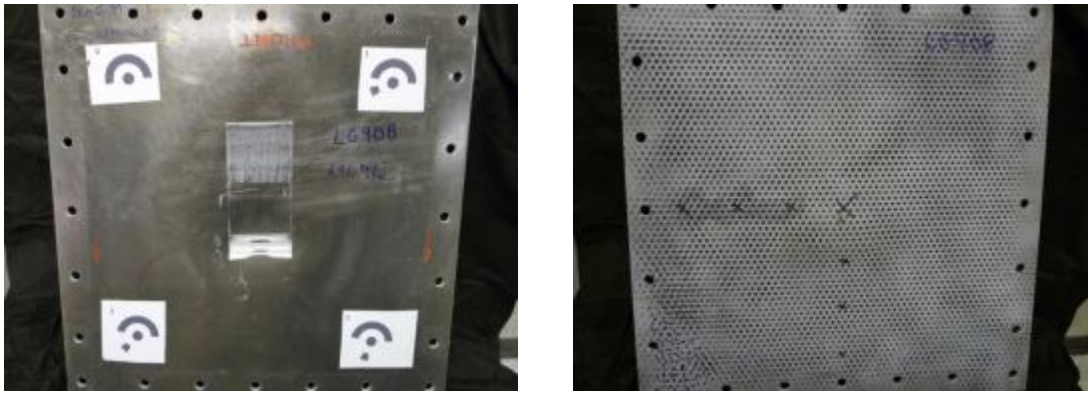

Figure 6. Front and back of the post-test panel in LG908

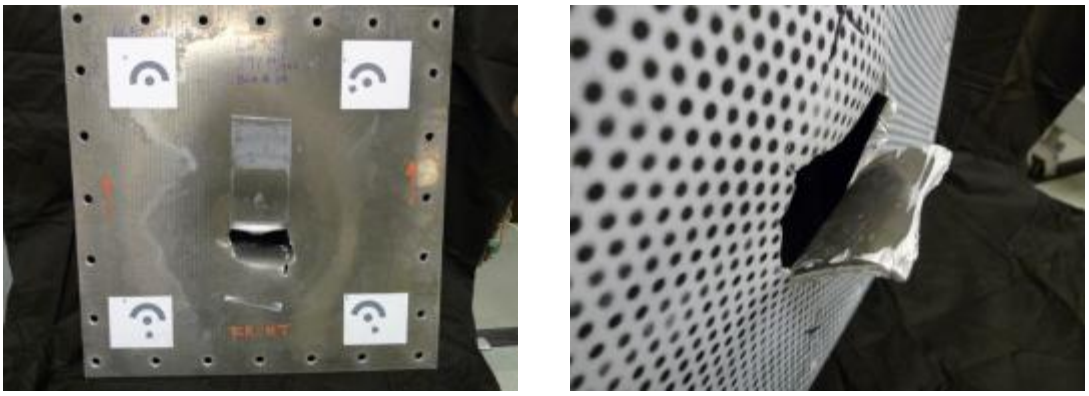

Figure 7. Front and back of the post-test panel in LG909

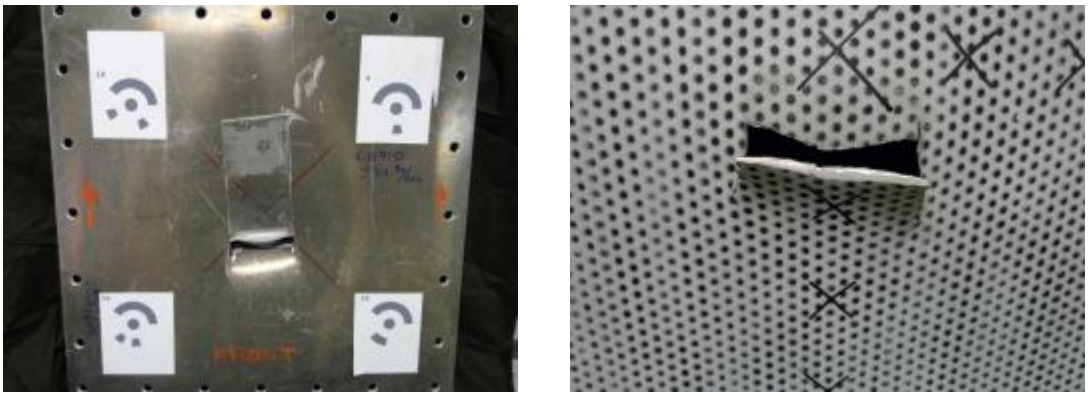

Figure 8. Front and back of the post-test panel in LG910

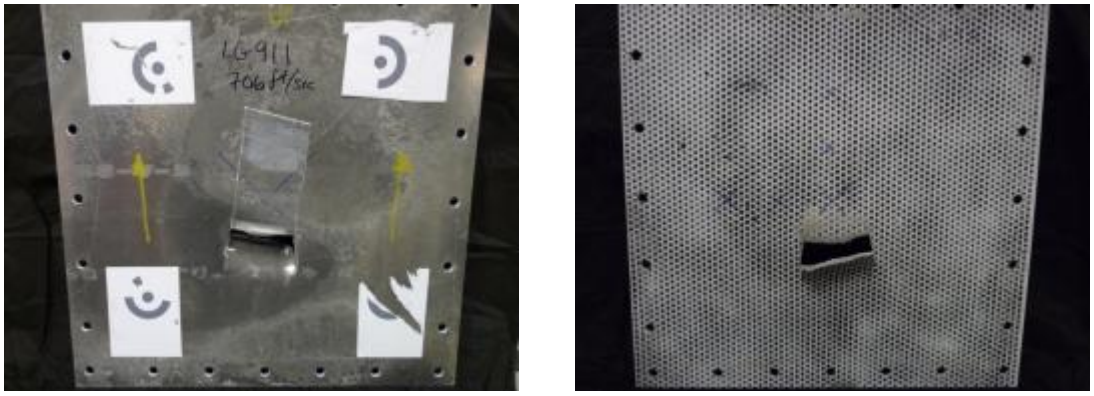

Figure 9. Front and back of the post-test panel in LG911

2.3 Summary

The progression of the blade projectile impact against the panel was essentially similar in all four tests, with the only exception being whether the blade root perforated the panel. In all cases, the tip of the blade projectile made the first contact on the panel, subsequently started bending, and the root rotated, impacting the panel. The root then scraped the panel surface generating deep gouges and ejecting significant wear debris. Since all tests were contained, the impact velocities in these tests were below the ballistic limit. However, there was perforation damage in some plates. For the discussion here, the onset of perforation damage will be referred to as the perforation critical velocity. When the impact velocity of the blade projectile was over this critical velocity, the panel was perforated at the side edge of the wear mark. The perforation propagated to make a wide opening with a large petal. However, in all four tests the blade projectile bounced back and fell away without penetrating the panel thoroughly.

Based on the photos of the post-test panels of LG909, LG910, and LG911 in Figure 7 through Figure 9, the shapes of the opening and petals are very similar to each other even though there were some variations of the 3D movements of the blade projectile among tests, as summarized in Table 1 and Table 2. Principally, the **X**-velocity is a dominant factor in this test, because that is the flight direction component of the projectile. The **X**-velocity of the projectile in LG908 was the lowest and the velocity in LG909 was the highest, with about a 100 ft/s difference. There was only about a 10 ft/s difference of the **X**-velocity of the projectile between LG908 and LG911, while the test results showed a distinct difference in the presence of the perforation. This means that under these impact conditions, the perforation critical velocity is in that range. The **Z**-velocity, pitch angle, and pitch velocity are also influential factors because they contribute to the rate of projectile root rotation onto the panel. Other components, such as Y-velocity, roll and yaw angles, and roll and yaw velocities, could be influential factors. However, their values and their variation ranges are relatively small in the tests. Their effects will be evaluated by comparing the simulations with half-symmetric and full FE models.

3 Blade impact FE models

Finite Element (FE) models were developed in LS-DYNA to simulate the NASA ballistic impact tests. The newly developed *MAT_224 material parameter set for Aluminum 2024 (version 2.2) (Park, Carney, Du Bois, Cordasco, & Kan, 2020) (Park, et al., 2020) (LS-DYNA Aerospace Working Group, 2021) was used to model plastic material failure behavior for the target Aluminum panel, and the *MAT_224 material parameter set for Titanium 6Al-4V (version 1.3) (Seidt, 2014) (LS-DYNA Aerospace Working Group, 2021) was used for the Titanium blade projectile. *MAT_224 is an elasto-visco-plastic material model that allows arbitrarily defined stress versus strain curves to define material plasticity, including arbitrary strain rate and temperature dependency. Adiabatic heating due to plastic work can cause temperatures to increase and the material to soften. Element erosion is included using plastic failure strain as a criterion and can be defined as a function of the state of stress, strain rate, temperature, and element size. This material model resembles the original Johnson-Cook material model (*MAT_015 in LS-DYNA) using similar separation of parameter dependencies, but with the possibility of general tabulated input parameters. The tabulated input parameters allow for a much closer match to mechanical property test data than the Johnson-Cook model, which is limited by curve fitting of the test data. In addition, *MAT_224 allows for parameter dependency of the Taylor-Quinney coefficient and regularization to reduce the mesh dependency of element erosion, the lack of which also limited the original Johnson-Cook model.

In a previous study (Park, et al., 2020), it was shown that the mesh size of an FE model using a *MAT_224 material model needs to be within the regularization range defined in that *MAT_224 input parameter set to get accurate failure behavior in a ballistic impact simulation. The allowable element size in the regularization range of *MAT_224, defined by an LCI table for Aluminum 2024 and Titanium 6Al-4V, is smaller than about 0.01 inch, which makes the full FE model required for this study about 82 million solid elements. In this study, the full FE model was developed and used for the NASA ballistic impact simulations. However, the full FE model is not practical for extensive studies because such a huge model requires excessive computer resources. Therefore, a half-symmetry FE model, which has about 41 million solid elements, was also developed for comparison of simulations. In addition, a coarse half-symmetric FE model, which has about 5 million solid elements with a 0.02-inch element size, was developed for the parametric study used to select appropriate modeling parameters, such as contact type, friction coefficient, and boundary condition. The reduced integration formulation for solid elements was used for all the simulations to help achieve a reasonable runtime.

3.1 Positioning and applying initial conditions

The following procedure was used to position the panel and the projectile in the model; refer to Figure 3 for the locations of the laboratory and the projectile local coordinate systems. The panel was initially positioned such that the face was perpendicular to the **X**-axis and the blade projectile was perpendicular to the **Z**-axis with its bottom face downward. Then, in the full FE model, the panel was rotated with a positive 45° angle around the **Y**-axis, and the blade projectile was rotated with a positive 45° angle around the $\mathbf{y_b}$-axis to make the angle between the panel and the blade projectile become a 90° angle, which was the original desired impact position. Since the actual measured position and orientation of the blade projectile at the moment of impact varied in the tests, the final position of the blade projectile was adjusted by implementing the computed roll, pitch and yaw Euler angles in $\mathbf{x_b}$-$\mathbf{y_b}$-$\mathbf{z_b}$ sequence in the blade local coordinate system. Then, all the initial conditions of the blade projectile, such as **X**-, **Y**- and **Z**- linear velocities and $\mathbf{x_b}$-, $\mathbf{y_b}$- and $\mathbf{z_b}$-angular velocities, were applied.

Applying initial conditions to the blade projectile in the full FE model was somewhat complicated. The complication stemmed from the fact that, in the tests, the movement of the blade projectile at the impact moment was computed using two different coordinate systems: its linear velocities in the global coordinate system and its angular velocities in the blade local coordinate system. The LS-DYNA keyword *INITIAL_VEHICLE_KINEMATICS gives a way to apply angular velocities to the blade projectile only in a global coordinate system. Therefore, the blade projectile had to be transformed to align the blade local coordinate system with the global coordinate system. Thus, the LS-DYNA keyword *INITIAL_VELOCITY can apply linear velocities to the blade projectile in the transformed global coordinate system.

In summary, it required a multi-stage transformation process to correctly position and define the correct initial conditions of the full FE model. First, the panel was positioned with a 45° slant around the **Y**-axis. Second, the blade projectile, which was initially positioned in a way to align the blade local coordinate system with the global coordinate system, was imported by taking transformations with the initial angular orientations (the roll, pitch and yaw Euler angles) in a $\mathbf{x_b}$-$\mathbf{y_b}$-$\mathbf{z_b}$ sequence in the blade local coordinate system. Third, the whole model, including both the panel and blade projectile, was transformed in the inverse of the second stage. This third step was completed in order to make the blade local coordinate system align with the global coordinate system again to apply angular velocities to the blade projectile, which would create the final full FE model.

For the half-symmetric FE model, half of the initially positioned full FE model was removed, imposing symmetry about the Y-axis. The final position of the blade projectile was created by

taking into account only the pitch Euler angle rotation around the $\mathbf{y_b}$-axis. Then, only **X**-linear velocity and $\mathbf{y_b}$-angular velocity were applied to the blade projectile.

In the half-symmetric FE model, applying initial conditions to the blade projectile is much simpler because only **X**-linear velocity and $\mathbf{y_b}$-angular velocity are applied to the blade projectile, and the $\mathbf{y_b}$-axis is already aligned with the **Y**-axis. So, the LS-DYNA keyword *INITIAL_VELOCITY_GENERATION can apply both **X**-linear velocity and $\mathbf{y_b}$-angular velocity to the blade projectile without any complicated transformations.

3.2 Contact parameters

The eroding surface contact was used between the panel and the blade projectile to maintain alignment of the contact surfaces between their interior elements after exterior elements had been eroded. The eroding contact parameters and their final values are listed in Table 3. The contact parameters for the preliminary runs used default values with a segment-based contact formulation (SOFT option=2 with SFS=1.0 in Table 3). Static and dynamic friction coefficients (FS and FD in Table 3) were set to a minimal 0.1, and 20% viscous contact damping (VDC in Table 3) was applied. In general, these values were retained throughout the study, but more realistic, higher friction coefficients were later found to be required to reproduce the impact physics.

Table 3. Parameters and their final values of the LS-DYNA keyword *CONTACT_ERODING_SINGLE_SURFACE (LSTC, 2017)

```
*CONTACT_ERODING_SINGLE_SURFACE
$     SSID      MSID     SSTYP     MSTYP    SBOXID    MBOXID       SPR       MPR
   1000000                 2
$       FS        FD        DC        VC       VDC    PENCHK        BT        DT
       0.3       0.3                           20.0
$      SFS       SFM       SST       MST      SFST      SFMT       FSF       VSF
      10.0
$     ISYM    EROSOP      IADJ
         0         1         1
$     SOFT    SOFSCL    LCIDAB    MAXPAR     SBOPT     DEPTH     BSORT    FRCFRQ
         2                                       2        23
```

VARIABLE	DESCRIPTION
SSID	Slave part set ID
SSTYP	ID type of SSID (EQ.2: Part set ID)
FS	Static coefficient of friction
FD	Dynamic coefficient of friction
VDC	Viscous damping coefficient in percent
SFS	Scale factor on default slave penalty stiffness when SOFT = 2
ISYM	Symmetry plane option (EQ.0: Off)
EROSOP	Erosion/interior node option (EQ.1: Storage is allocated so that eroding contact can occur)
IADJ	Adjacent material treatment for solid elements (EQ.1: Solid element faces are included if they are on the boundary of the material subset. This option also allows for erosion within a body and the subsequent treatment of contact)
SOFT	Contact formulation EQ.0: Penalty formulation EQ.1: Soft constraint formulation EQ.2: Segment-based contact
SBOPT	Segment-based (SOFT = 2) contact options EQ.2: Assume planer segments (default) EQ.3: Warped segment checking EQ.4: Sliding option EQ.5: Do options 3 and 4
DEPTH	Search depth in automatic contact to check for nodal penetration through the closest contact segments. EQ.2: Check surface penetration only (default) EQ.3: Check surface penetration but measure depth of penetration at segment edges as well as nodes EQ.5: Check surface penetration and also edge to edge penetration EQ.13: Similar to 3, but tuned to conserve energy EQ.23: Similar to 3, but search is based on segment overlap calculation EQ.25: Similar to 5, but search is based on segment overlap calculation EQ.33: Similar to 23, but with modifications to improve robustness EQ.35: Similar to 25, but with modifications to improve robustness EQ.45: Splitting pinball method of Belyschko and Yeh

The preliminary impact simulations with the initial contact parameters showed a contact problem between the panel and blade projectile. Figure 10 shows the energy balance plots of the ballistic impact simulation of LG908 using the half-symmetric coarse FE model. The contact energy needed to prevent penetration between the contact partners can be obtained by subtracting the friction energy from the sliding interface energy because the sliding interface energy includes both the friction and contact energies. Contact forces that prevent mutual penetrations of the projectile and panel FE meshes during the impact should be equal and opposite, and balance out. However, numerical contact algorithms cannot do this perfectly, and so non-physical contact energy will be generated in practical FE analyses. The contact energy should be small enough to not affect the overall results of the simulation. It can be observed that the maximum contact energy is about 10% of the maximum internal energy.

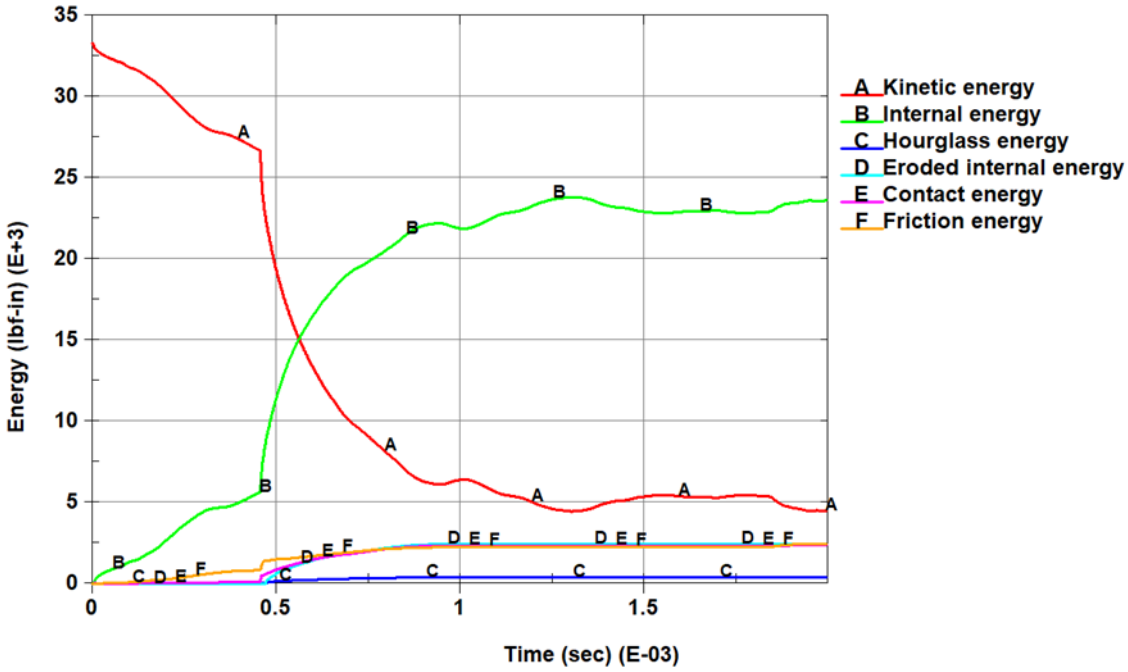

Figure 10. Energy balance plots of the simulation of LG908 using the half-symmetric coarse FE model with the initial contact parameters

In general, 10% of internal energy could be considered acceptable for the contact energy in many applications. However, a more stringent criterion was taken in this research because the contact between the panel and the blade projectile played a critical role in failure initiation on the panel. The root bottom edge of the blade projectile impacts the surface of the panel with a considerable impulse and slides down the panel with uneven contact force, similar to mechanical chatter. The contact interface between the projectile and the panel becomes very uneven and sharp due to

eroded elements on both sides, making the contact algorithm inefficient and allowing penetration. In addition, some penetrations were observed in the simulations.

In order to find the best contact parameters to minimize the contact energy, a contact parameter study was conducted. First, all the possible combinations with three parameters, SOFT, SBOPT and DEPTH, were run and their contact energies were compared. The results showed that the cases with SOFT=2 and DEPTH=23 had smaller contact energy than the initial simulation, and the case with SOFT=2, SBOPT=2, and DEPTH=23 had the smallest contact energy among them. Figure 11 shows the energy balance plots of the simulation with modified contact parameters. The contact energy is about 8.3% of the internal energy.

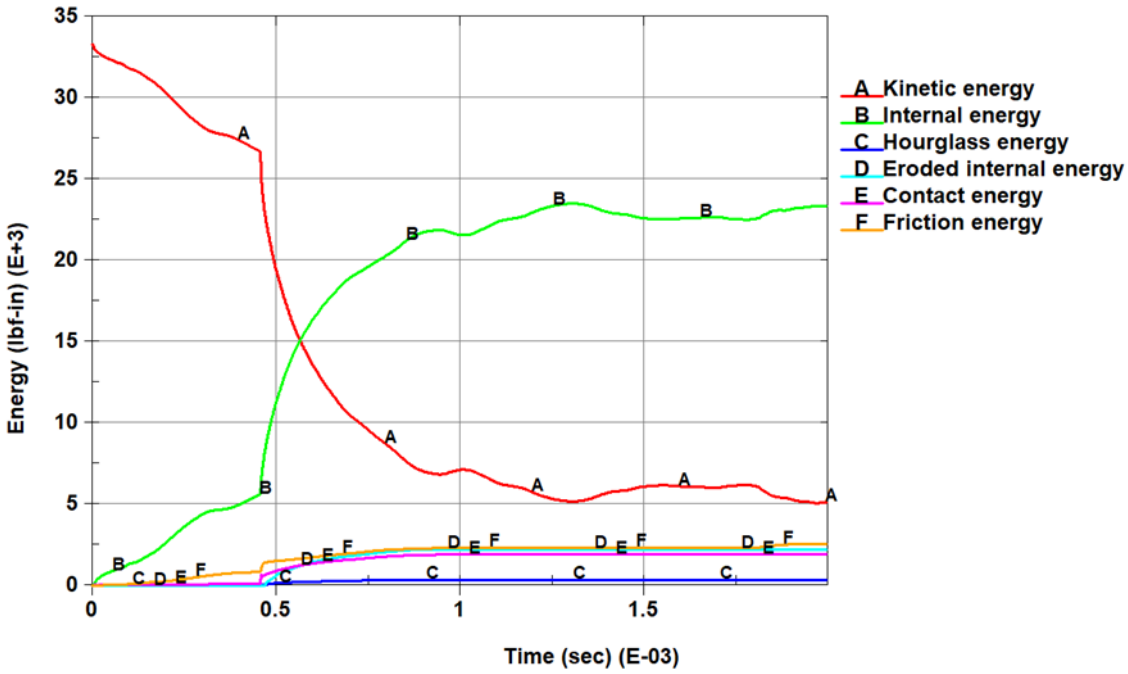

Figure 11. Energy balance plots of the simulation of LG908 using the half-symmetric coarse FE model with modified contact parameters (SOFT=2, SBOPT=2, and DEPTH=23)

The contact energy was further reduced by making the contact penalty factor (SFS), which provides a means of increasing the contact stiffness. Figure 12 shows the energy balance plots of the simulation with the modified contact parameters and higher contact penalty factor (SFS=10.0). In this case, the contact energy is now only about 1.2% of the internal energy. Since the contact stiffness became much higher, the numerical stability of the FE model was checked by varying the scale factor for computed time step (TSSFAC) of the LS-DYNA keyword *CONTROL_TIMESTEP. The initial TSSFAC was 0.7 and its lower values were tried. The

difference among the simulations with different TSSFAC values are minimal. Therefore, the TSSFAC was set to 0.7 for all the simulations.

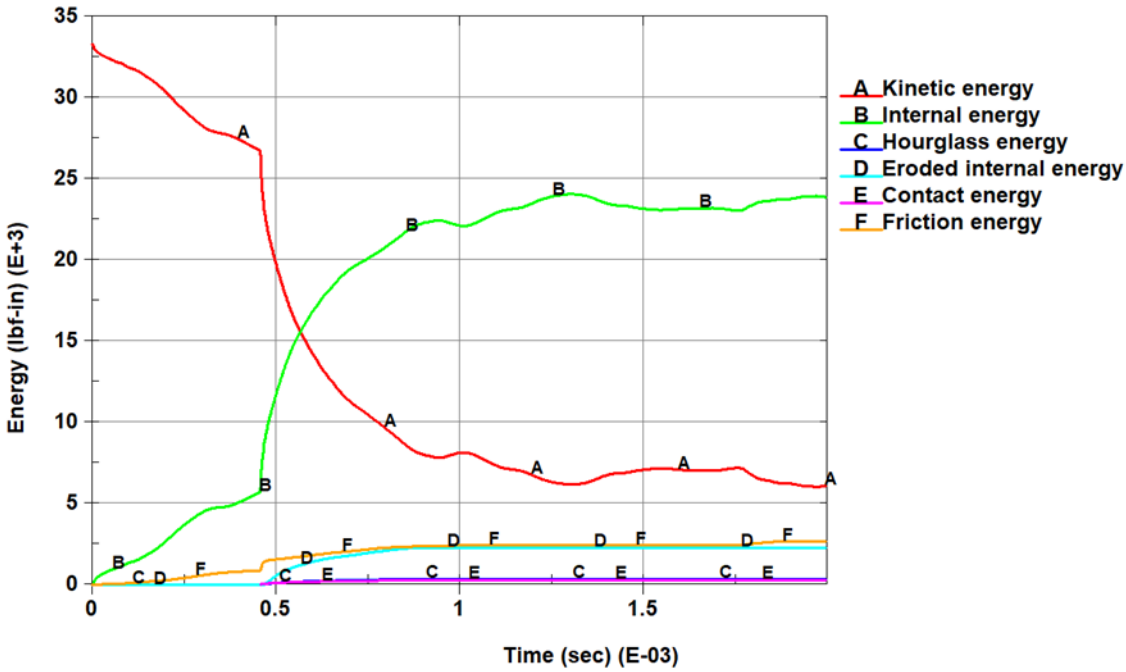

Figure 12. Energy balance plots of the simulation of LG908 using the half-symmetric coarse FE model with modified contact parameters (SOFT=2, SBOPT=2, and DEPTH=23) and higher contact penalty factor (SFS=10.0)

3.3 Contact friction

The preliminary simulation of the LG909 test was conducted using the half-symmetric coarse FE model with 0.1 contact friction coefficients (FS and FD in Table 3). In extreme conditions, friction coefficients are difficult to accurately determine, vary not only with material but also with force and velocity, and so are often set low to minimize their effect on an analysis. In this study, a set of simulations was conducted where the static and dynamic coefficients were varied in a range from 0.1 to 0.5. The static and dynamic coefficient were set to the same value for each simulation (FS=FD). Typically, static coefficients of friction are higher than dynamic coefficients of frictions. However, impact simulations are not as sensitive to the static coefficient of friction as they are to the dynamic coefficient. In order to reduce complications, the values were held identical.

As shown in Figure 7, test LG909 showed perforation of the panel by the blade projectile. However, no perforation was predicted in the preliminary simulation. Figure 13 shows the

vertical cross-section view of the simulation of the LG909 test at 1.8 inches away from the panel center, at the moment that the blade projectile is sliding down while scraping the surface of the panel. The enlarged image of the sliding area between the panel surface and the bottom root of the blade shows that many solid elements in both the panel and blade projectile were eroded by the impact, which made both contact surfaces jagged. In the tests, huge impact and frictional forces caused the considerable wear and erosion that occurred at the impact areas of both panel and the blade projectile, and eventually caused the perforation in the panel. Comparing test and analysis, the damaged test hardware surfaces exhibit both wear and erosion due to tribochemical processes (Dong & Bell, 1999) (Mishra, 2014) and plastic deformation, providing better conformity to one another and resulting in greater contact surface area. In contrast, the contacting elements in the model eroded resulting in jagged point and edge contacts at the contact interface. The jagged contact surfaces in the model greatly reduced the contact surface area, which strongly affected the predicted contact frictional force and played a critical role in predicting whether the panel was perforated.

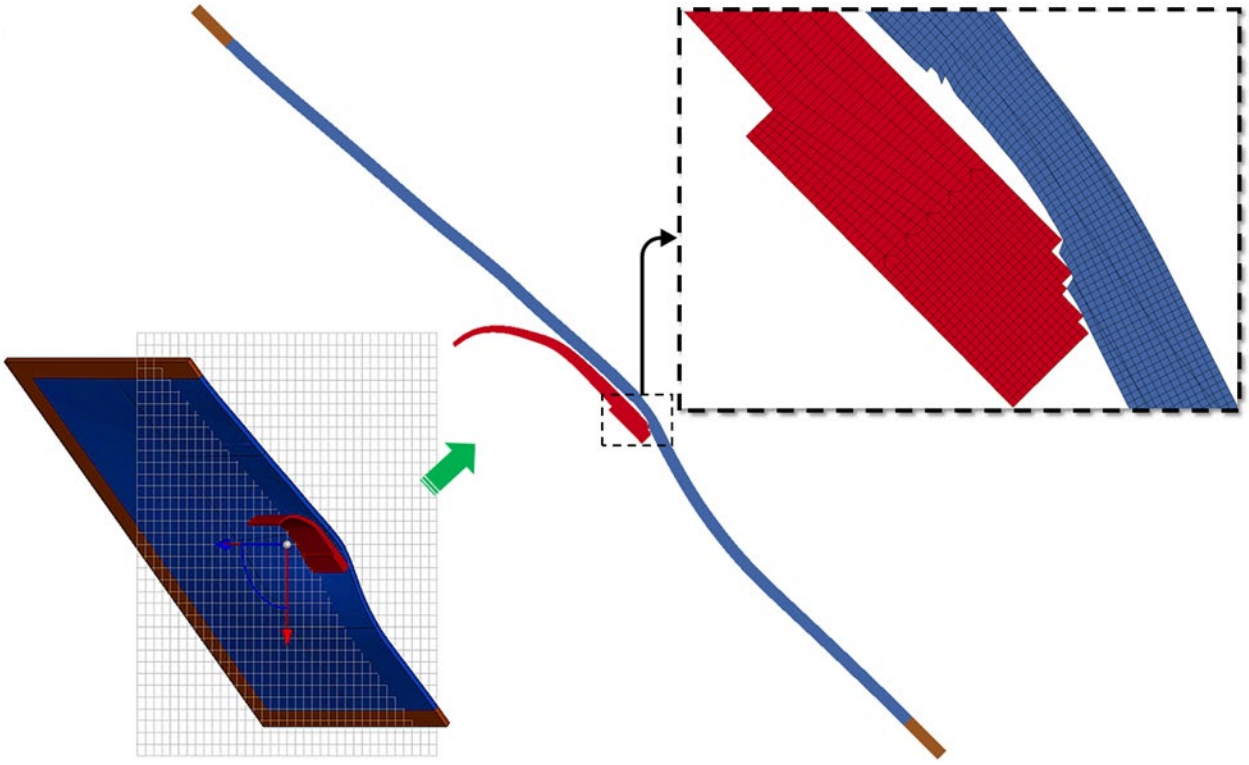

Figure 13. Vertical cross-section view of the simulation of the LG909 test at 1.8 inches away from the panel center at the moment when the blade projectile is sliding down while scratching the surface of the panel (FS=FD=0.1)

In order to study the effects of the contact friction, the contact friction coefficients (FS and FD in Table 3) were varied. Figure 14 shows the enlarged impact area of the vertical cross-section view of the simulation (with the half-symmetric coarse FE model) of the LG909 test with 0.5 contact friction coefficients. It can be observed that the increased contact friction made the surface wear and erosion on the panel deeper, which initiated the failure at the back surface of the panel, as shown in Figure 14(a). Then, it caused the initial perforation in the panel as seen in Figure 14(b). These analytical results are a much closer match to the test results, in both the blade to panel conformity and the perforation.

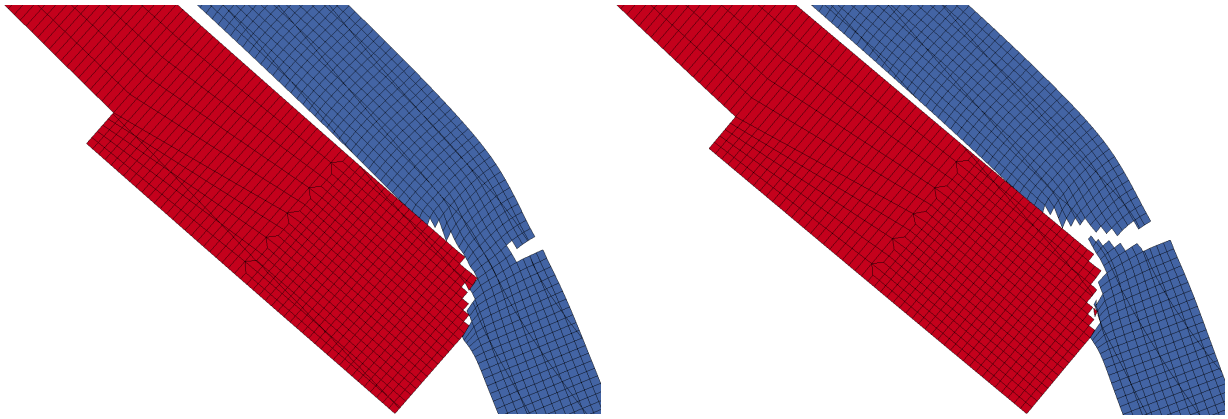

(a) (b)

Figure 14. Enlarged impact area of the vertical cross-section view of the simulation (with the half-symmetric coarse FE model) of the LG909 test at 1.8 inches away from the panel center at the moment when the blade projectile is sliding down while scratching the surface of the panel (FS=FD=0.5): (a) failure initiation at the back surface of the panel and (b) initial perforation

The higher contact friction coefficients and resulting solid element erosion created the closer match to the conditions that were observed in the tests. These higher friction coefficient values of 0.5 are within the wide spread of published friction coefficients for Ti-64 (Dong & Bell, 1999). The resulting element erosion is a closer match to observed Ti-64 wear than the jagged contact that results from using a low 0.1 friction coefficient. The wear and erosion that result from the tribochemical effects are significant contributors to Ti-64 friction physics. Note that these tribochemical processes are not being modeled, and the closer match is being achieved by element erosion using an effective plastic strain criterion.

Element erosion and contact friction are significant contributors to the accuracy of the Ti-64 projectile impacting plate simulations. Any solid element erosion is element size dependent, since it is discrete elements that are being removed from the problem. As a result, the contact friction coefficients that are used in conjunction with element erosion are also dependent on mesh size. The smaller the mesh size is, the smoother the contact surface remains after element

erosion, which then requires smaller contact friction coefficients. Figure 15 shows the enlarged impact area of the vertical cross-section view of the simulation (with the half-symmetric fine FE model) of the LG909 test with 0.3 contact friction coefficients. Comparing Figure 15 with Figure 14, it can be observed how the different mesh size and friction coefficients would affect the processes of wear, erosion, and perforation between the blade and panel.

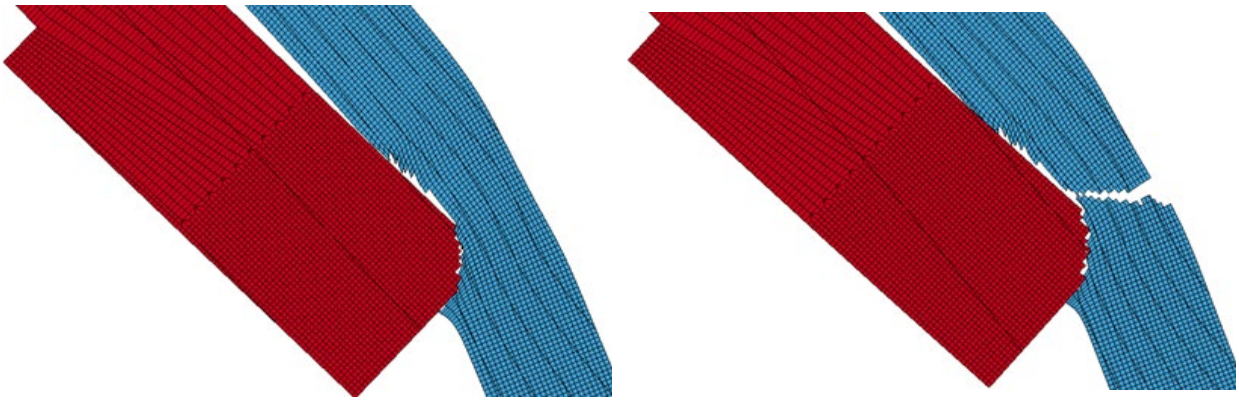

(a) (b)

Figure 15. Enlarged impact area of the vertical cross-section view of the simulation (with the half-symmetric fine FE model) of the LG909 test at 1.8 inches away from the panel center at the moment when the blade projectile is sliding down while scratching the surface of the panel (FS=FD=0.3): (a) right before perforation initiation and (b) initial perforation

3.4 Boundary condition

In order to check if the boundary condition was working appropriately in the simulations, the deformation profile of the central vertical cross-section of the panel at the maximum displacement moment was compared with the LG908 test, where the panel was not perforated. The deformation was measured in the local panel coordinate system from the DIC of the back surface of the panel in the tests. The origin of the panel coordinate system is located in the center of the back surface of the panel, the $\mathbf{x_p}$-axis faces downward parallel to the back surface of the panel, and the $\mathbf{z_p}$-axis faces vertically outward of the back surface of the panel, as shown in Figure 16. As the blade projectile rotated in flight, the impact locations of the blade projectiles on the panel varied from test to test, so the maximum points of the deformation profiles were shifted to align them to match.

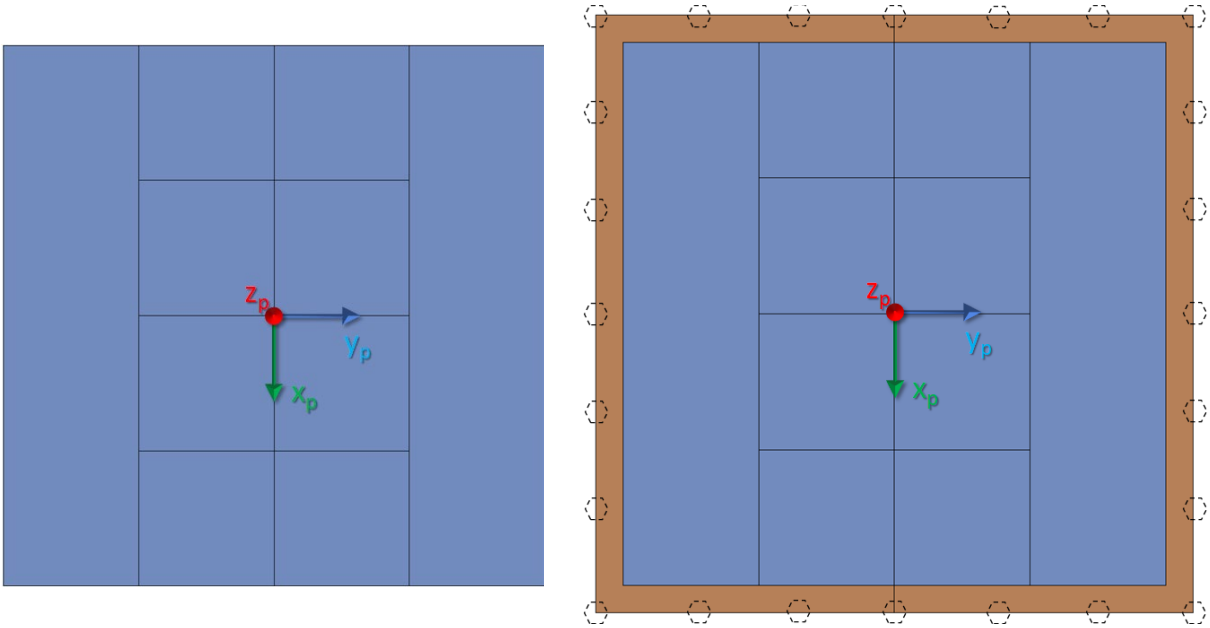

(a) (b)

Figure 16. Back surface of the panel FE models: (a) without a boundary area and (b) with a 0.5-inch boundary area

Initially, a simple boundary condition for the panel, called BC1, was set such that all the Degrees of Freedom (DOFs) of all the edge surfaces of the panel were fixed without modeling the 1.0-inch fixture area. This serves to constrain the vertical and lateral movements at the panel boundaries in the panel coordinate system, as is shown in Figure 16(a). Figure 17 compares the deformation profiles of the central vertical cross-section of the panel of the LG908 test and simulation using the half-symmetric coarse FE model with BC1 at the maximum displacement moment. The maximum deformation of the LG908 test is about 1.2 inches. The deformation profile of the simulation is similar in shape to the test, but its maximum deformation is about 0.2 inches (20%) smaller. Given the profile similarity of the test and simulation, a probable explanation of the difference is that BC1 over-constrained the panel.

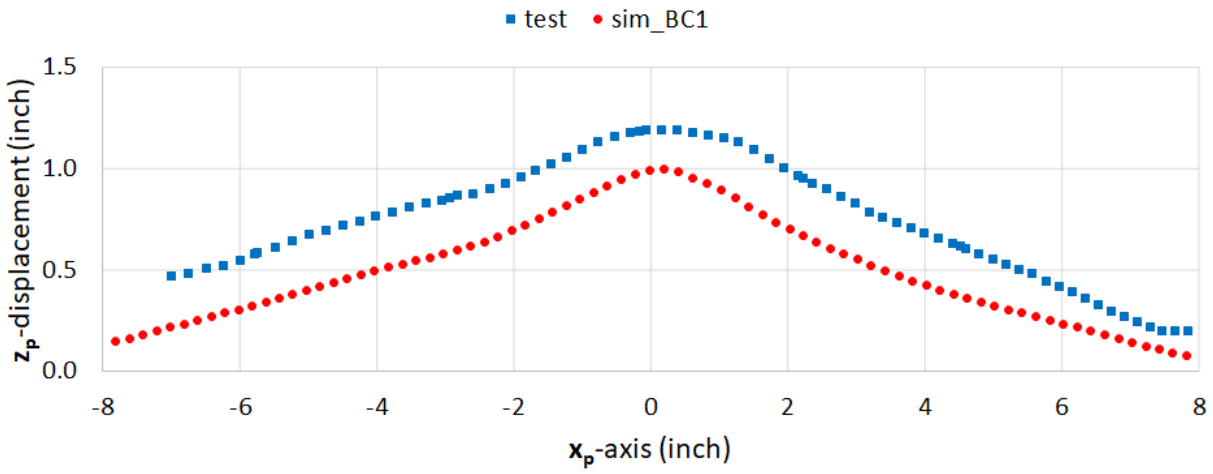

Figure 17. Comparison of deformation profiles of the central vertical cross-section of the panel of LG908 test and simulation using the half-symmetric coarse FE model with BC1 at the maximum displacement moment

A second boundary condition, termed BC2, applied only $\mathbf{z_p}$-DOF fixed constraints to all the edge surfaces of the panel. Therefore, the vertical movement of the panel boundaries in the panel coordinate system was constrained, but their lateral movement was released. Figure 18 compares the deformation profiles of the central vertical cross-section of the panel of the LG908 test and simulation using the half-symmetric coarse FE model with BC2 at the maximum displacement moment. It shows that the maximum deformation of the simulation with the BC2 is about 0.2 inches (20%) larger than the test, as opposed to the simulation with the BC1.

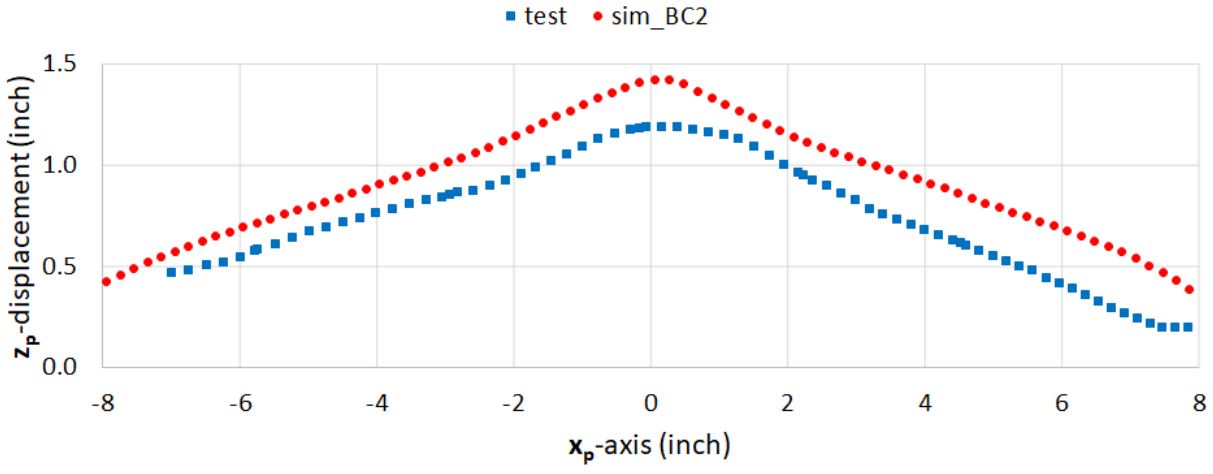

Figure 18. Comparison of deformation profiles of the central vertical cross-section of the panel of LG908 test and simulation using the half-symmetric coarse FE model with BC2 at the maximum displacement moment

In a third case, BC3, a 0.5-inch fixture area was added in the panel FE model, and the front and back surfaces of the fixture area were fixed in only $\mathbf{z_p}$-DOF. In addition, the $\mathbf{x_p}$-DOF of the left and right bolt areas and the $\mathbf{y_p}$-DOF of the top and bottom bolt areas were fixed to prevent lateral rigid-body motion of the panel. Figure 16(b) shows the 0.5-inch fixture area in brown and 24 bolt locations by dashed hexagon symbols. Figure 19 compares the deformation profiles of the central vertical cross-section of the panel of the LG908 test and simulation using the half-symmetric coarse FE model with BC3 at the maximum displacement moment. It shows that the maximum deformation of the simulation with the BC3 is about 0.1, inches (8.3%) smaller than the test, which was less than a 10% difference and is considered acceptable. So BC3 was used for all subsequent simulations.

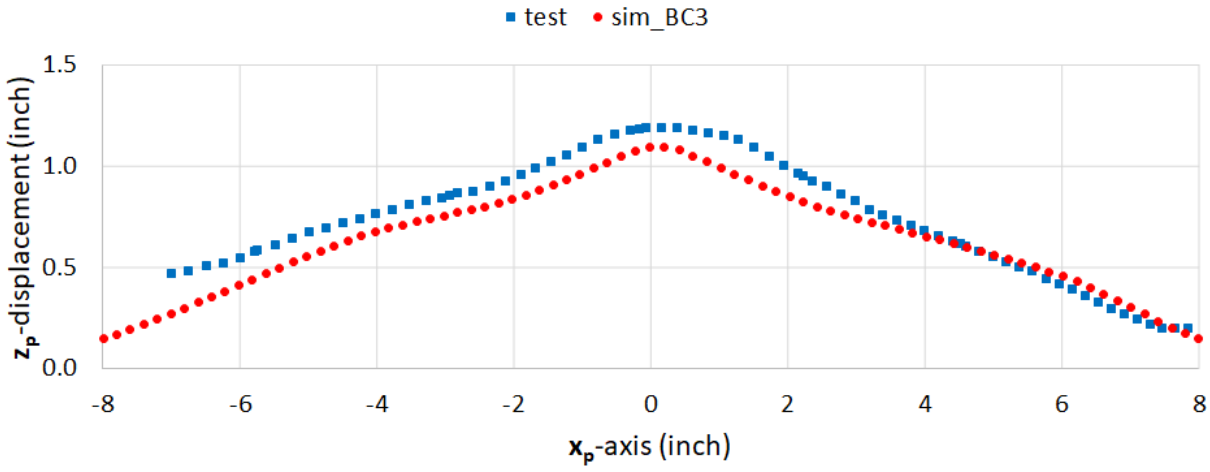

Figure 19. Comparison of deformation profiles of the central vertical cross-section of the panel of LG908 test and simulation using the half-symmetric coarse FE model with BC3 at the maximum displacement moment

4 Blade impact simulations

The ballistic impact simulations of all four tests were conducted using LS-DYNA. Both half-symmetric and full FE models developed in Section 3 were used for comparison to see the effects of the roll and yaw motions of the blade projectile. In the full FE model, all the initial roll, pitch and yaw angles of the blade projectile in Table 2 were implemented, and all three directional linear velocities and angular velocities of the blade projectile in Table 1 and Table 2 were applied. In the half-symmetric FE model, however, only the pitch angle, **X**-velocity and pitch angular velocity of the blade projectile were considered. The contact friction coefficients (FS and FD) were set to 0.3 because the mesh size of the FE models is smaller than the coarse FE model used for the contact parametric study. The simulation results are shown below.

4.1 LG908

The blade projectile posture at the impact moment of the LG908 test is shown in Figure 20(a). The initial setups of the ballistic simulations of LG908 using the half-symmetric and full FE models are shown in Figure 20(b) and Figure 20(c), respectively. The **X**-velocity of the projectile is 712.8 ft/s, which is the lowest of all four tests.

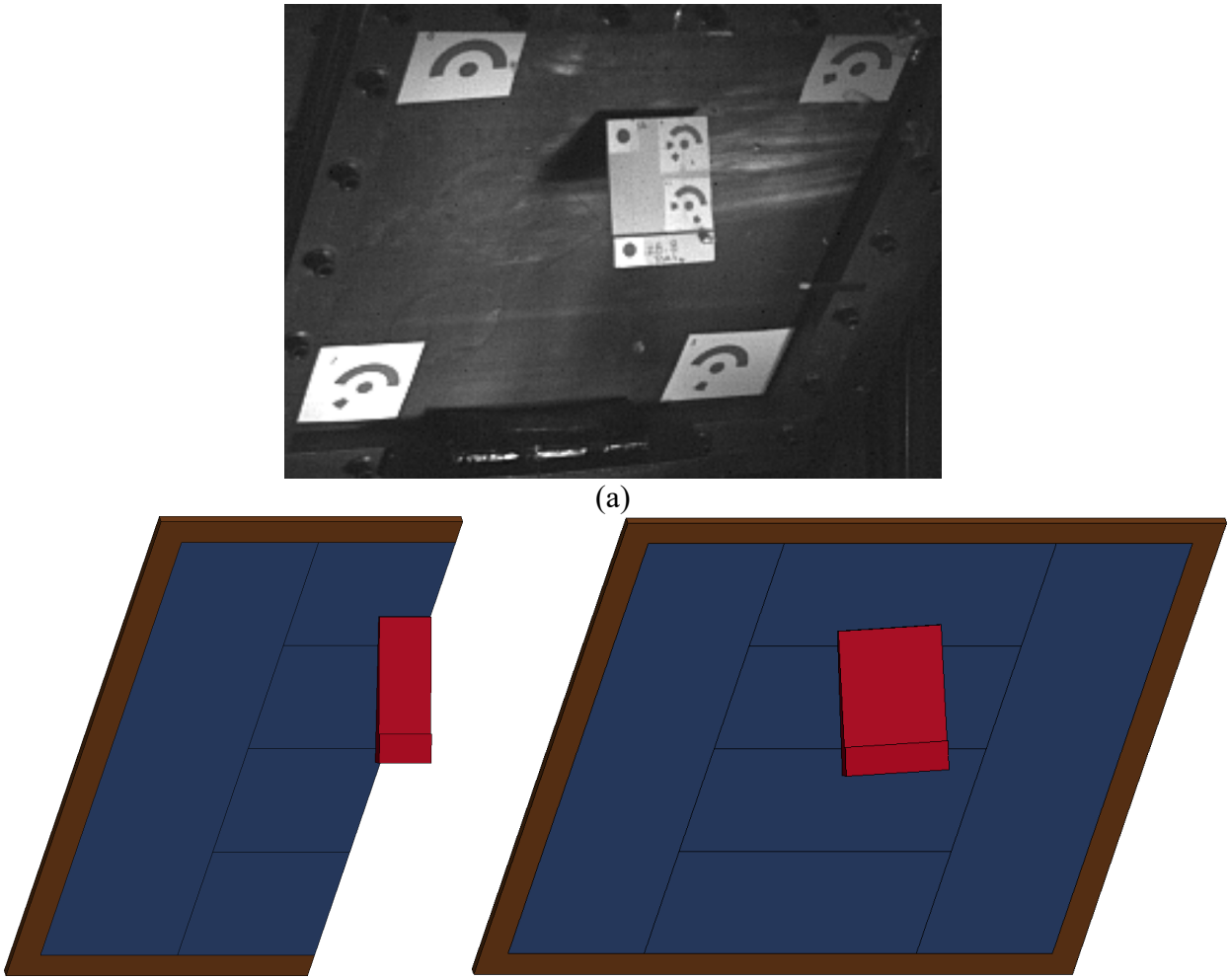

(a) (b) (c)

Figure 20. The blade projectile posture at the impact moment of the LG908: (a) test, (b) simulation using the half-symmetric FE model, and (c) simulation using the full FE model

The panel deformation in the LG908 test is shown in Figure 21(a). No perforation of the panel occurred by the impact of the blade projectile in LG908. Instead, the hard contact of the bottom root of the blade projectile to the panel surface made a large wear mark on the panel surface. Figure 21(b) and Figure 21(c) show the panel deformations of LG908 simulations in an effective plastic strain contour using the half-symmetric and full FE models, respectively. Similar to the test, no perforation occurred in either simulation. There is no noticeable difference between the

two simulations, except for the slightly rotated impact marks of the blade projectile in the simulation using the full FE model due to the roll and yaw rotations of the blade projectile.

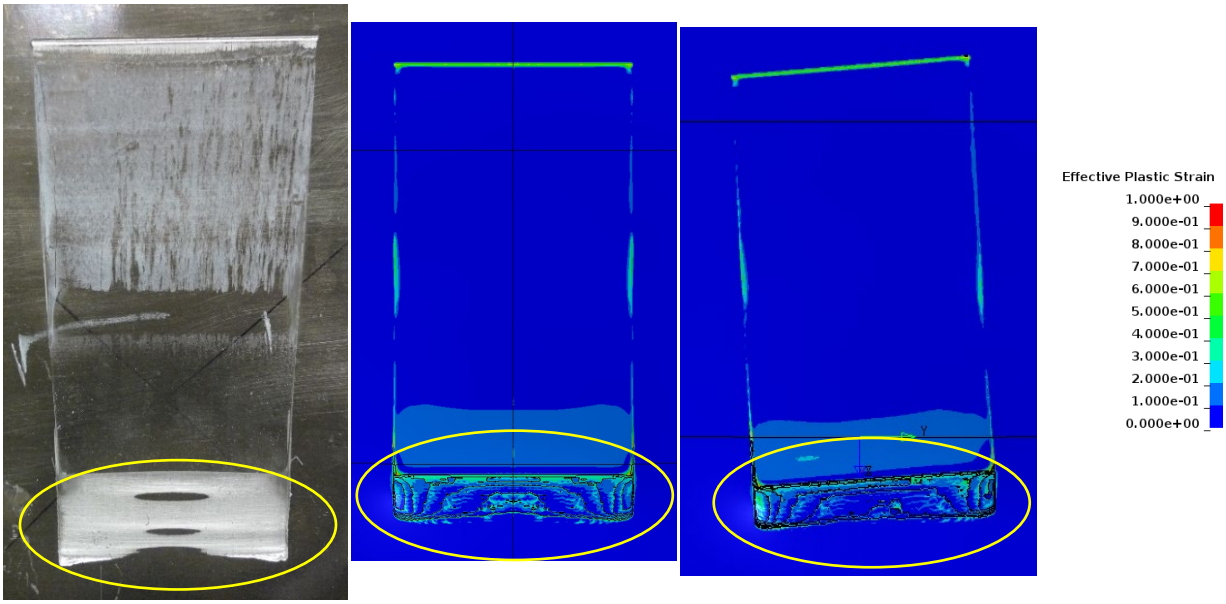

(a) (b) (c)

Figure 21. Panel deformation in LG908: (a) test (b) simulation at 2 msec using the half-symmetric FE model, and (c) simulation at 2 msec using the full FE model

The main difference between the test and simulations is the vertical length of the wear mark created by the blade root. The wear mark in the test is almost two times longer than the one in the simulations, which is highlighted in Figure 21 with a yellow circle. As shown in Figure 5 in Section 2, many debris particles were avulsed when the blade projectile scraped on the panel surface in the LG908 test. In the simulations, however, all the elements at the wear area are eroded and no element debris falls away. This means that an additional portion of the impact energy of the blade projectile was spent eroding these elements, many of which should have become debris. This may be a reason why the wear marks in the simulation are shorter than the one in the test. Additionally, necessarily using contact friction coefficients rather than modeling the actual tribochemical friction process, unavoidably adds uncertainty and inaccuracy to the analysis.

The deformation of the blade projectile in the simulations is shown in Figure 22. Unfortunately, they could not be compared with the one in the test because the photos of the post-test blade projectile in the test were not available. In the simulations, it can be seen that the tip area of the blade projectile was bent by its rolling on the panel surface, and some elements in the root bottom edge of the blade projectile were eroded by wear of the contact and frictional sliding on the panel surface, especially at the corners.

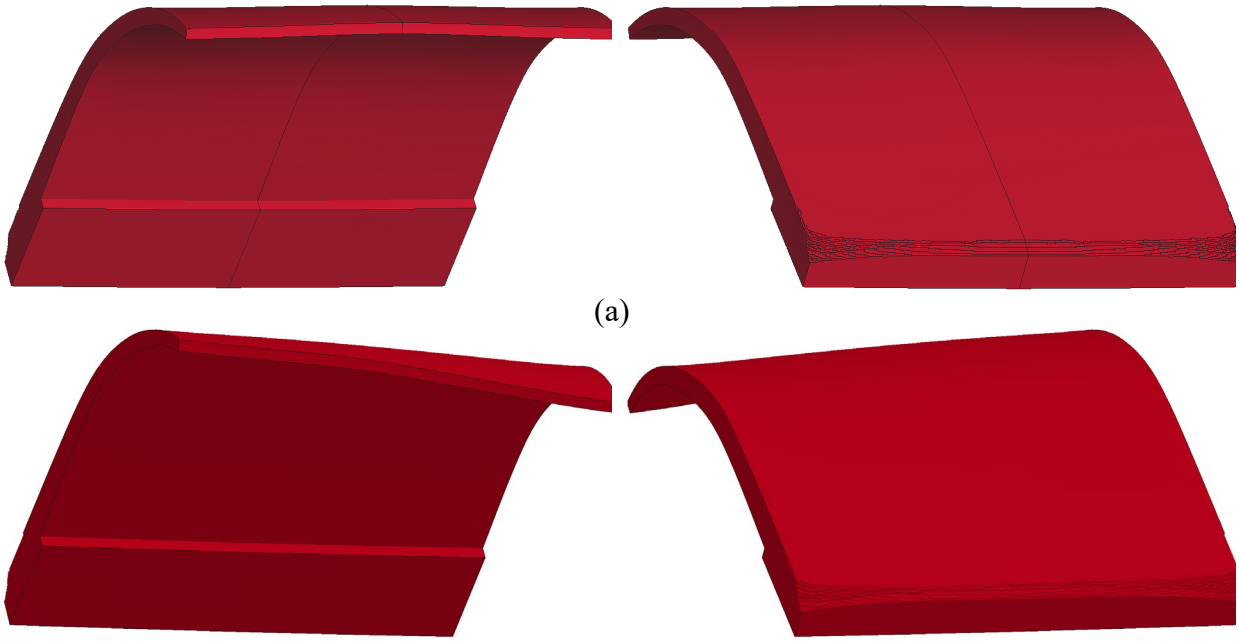

(a)

(b)

Figure 22. Deformation of the blade projectile at 2 msec in LG908: (a) simulation with the half-symmetric FE model and (b) simulation with the full FE model

Figure 23 shows the energy balance plots of the simulations of LG908, confirming that the hourglass energy and contact energy (obtained by subtracting the friction energy from the sliding interface energy) are very small. The eroded internal energy, which is spent for element erosion in the panel and blade, takes about 18% of the internal energy.

The element erosion is the typical implementation of the material failure of many constitutive models in LS-DYNA including *MAT_224. The element deletion by this approach raises the essential problem of losing both mass and energy in the global system. In general, however, this element deletion method has been successful in many applications where these losses are small enough and not critical to the system. In these ballistic impact simulations, the mass loss caused by the element erosion is less than 2% of the mass of the blade projectile. On the other hand, the energy loss reaches about 18% in LG908, which is not ignorable.

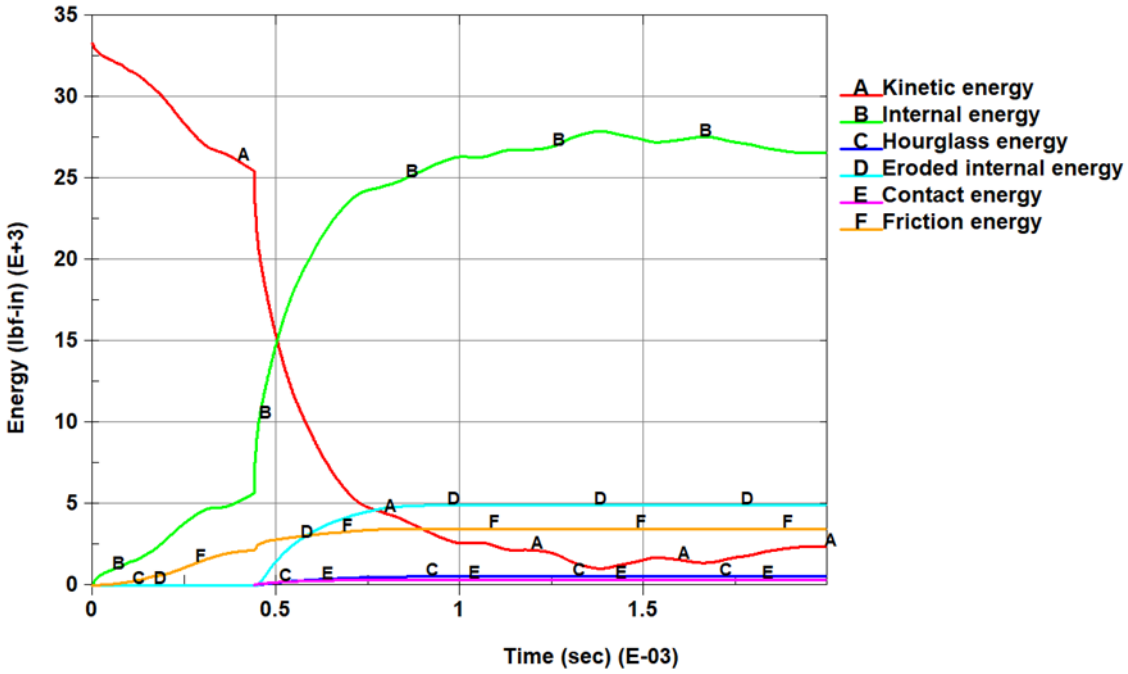

(a)

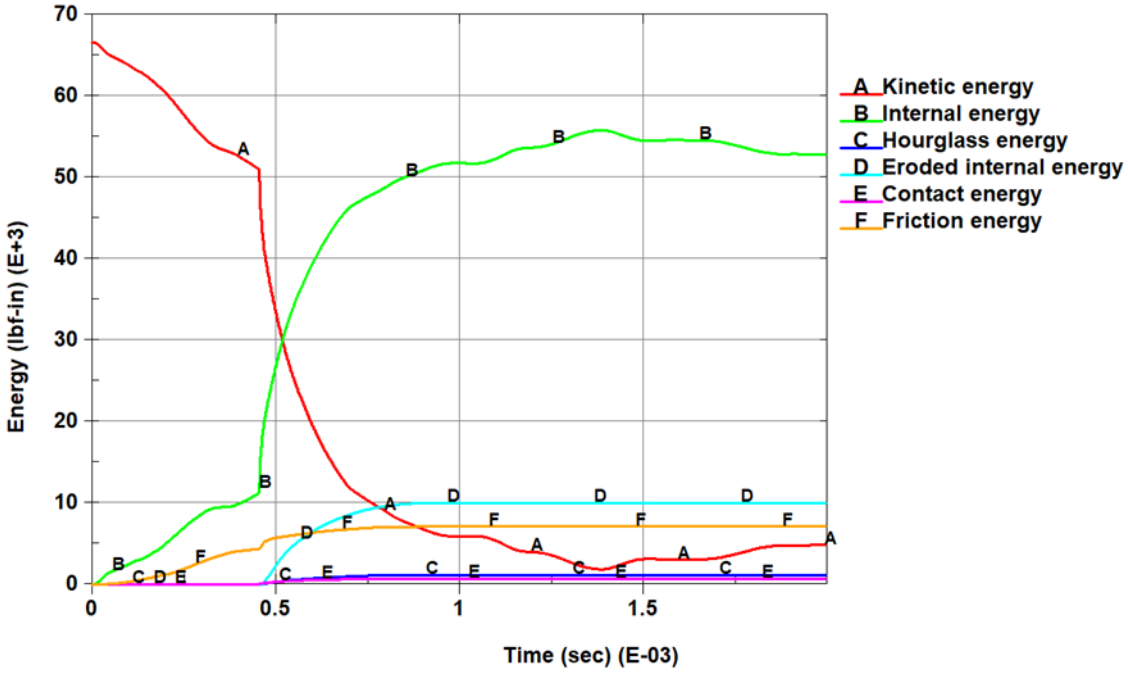

(b)

Figure 23. Energy balance plots of the simulations of LG908: (a) the half-symmetric FE model and (b) the full FE model

The impact process of the blade projectile on the panel was divided into three stages in order to compare their deformation profiles of the central vertical cross-section of the panel between the test and simulations. Table 4 describes the three stages: the first stage is at the time right before the root of the blade projectile impacted the panel; the second stage is after 0.09msec from the first stage, which is the same time interval between the first and the second stages in LG909; the third stage is at the time when the panel deformation reached the maximum. Recall that perforation does not occur in this test (LG908); this second stage is delineated here in order to compare with the higher velocity test (LG909). The timings of each stage are very closely aligned between the test and simulations.

Table 4. Three stages of the impact process of the blade projectile on the panel in LG908

LG908	**Test**	**Simulation**		**Note**
		Half-symmetric FE model	**Full FE model**	
Stage1	0.44 msec	0.44 msec	0.45 msec	Root impact
Stage2	0.53 msec	0.53 msec	0.53 msec	0.09 msec after Stage1 (Test)
Stage3	1.50 msec	1.48 msec	1.50 msec	Max displacement

The comparison of the deformation profiles of the central vertical cross-section of the panel between the test and simulation at each stage of LG908 is shown in Figure 24. In Stage1, they are almost identical. However, note that the Stage1 root impact using the full FE model occurred 0.01 msec later than the test and the half-symmetric simulation. In Stage2, the deformation profile of the simulation with the half-symmetric FE model is very close to the one in the test, but the deformation profile of the simulation with the full FE model is a little lower than the one in the test, probably due to the 0.01 msec time delay in Stage1. In Stage3, the deformation profiles between the test and both simulations are similar but show some differences in terms of their peak and peak shape. The peak of the deformation profile in the simulation with the half-symmetric FE model is 5% lower than in the test, which is better than the 8.3% lower prediction with the coarse half-symmetric FE model discussed in Section 3.4. The peak in the simulation with the full FE model is a little higher than the peak predicted with the half-symmetric FE model, but is still lower than the peak measured in test. The shape of the deformation profile at the peak response in the test is blunt, but the shapes predicted in both simulations is sharp. This difference could be due to the shorter wear area in the simulation. Had the root of the blade projectile scraped the panel surface long enough, it may have resulted in prediction of a blunt peak deformation profile at the central vertical cross-section of the panel.

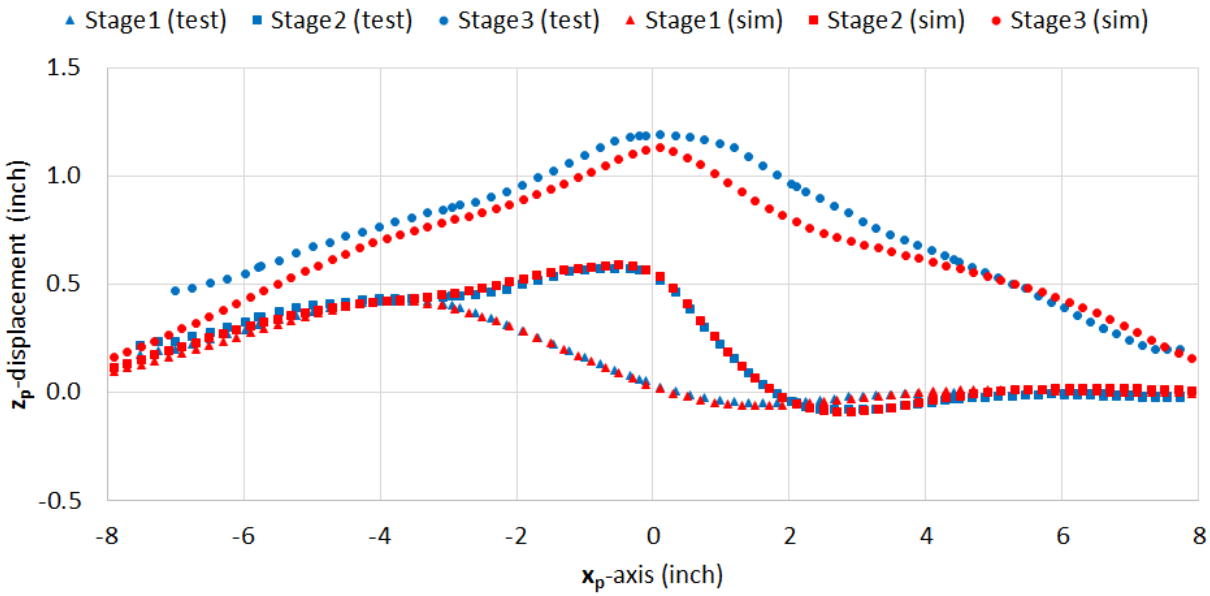

(a)

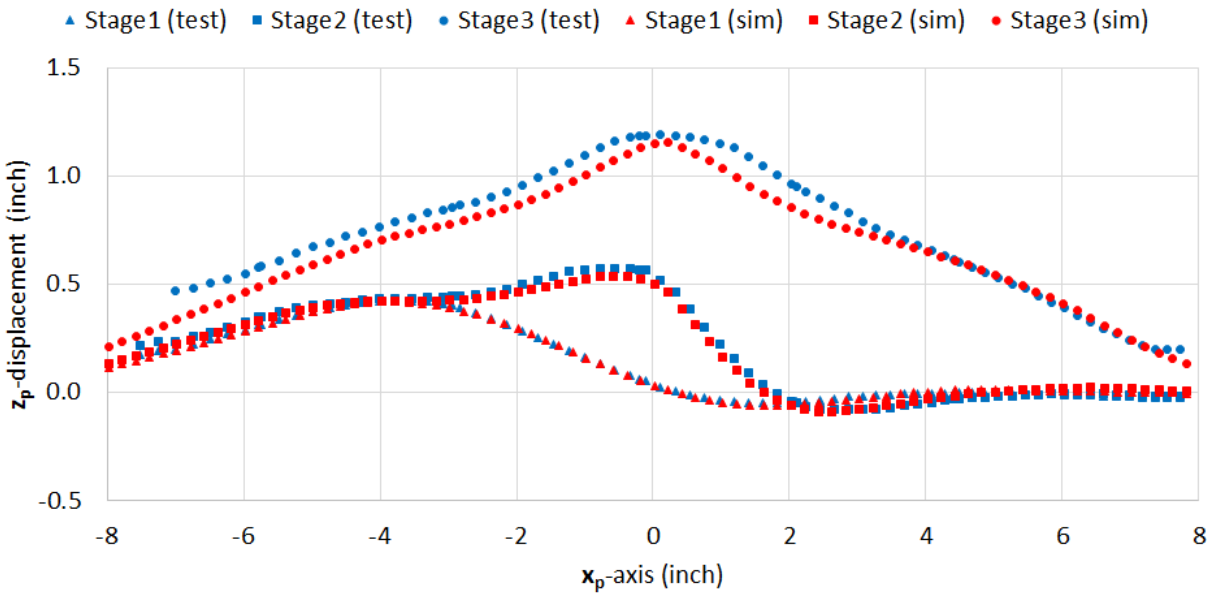

(b)

Figure 24. Comparison of deformation profiles of the central vertical cross-section of the panel in LG908: (a) simulation with the half-symmetric FE model and (b) simulation with the full FE model

The test and simulation displacement-time curves of the panel's back surface maximum displacement point are compared up to 2 msec, and are shown in Figure 25. There is a small difference in the shapes of the first peak between the simulations with the half-symmetric and full FE models. The peak shape of the displacement curve in the simulation with the half-

symmetric FE model is flat, probably because the whole root edge of the blade projectile impacts the panel at once, but with the full FE model it keeps increasing with a gentle slope, possibly because the blade root impacts the panel from one corner to the other due to the 3D rotation of the blade projectile. The displacement curve in the simulation with the full FE model is closer to the test. However, both displacement curves of the simulations are close enough to the test to be considered acceptable.

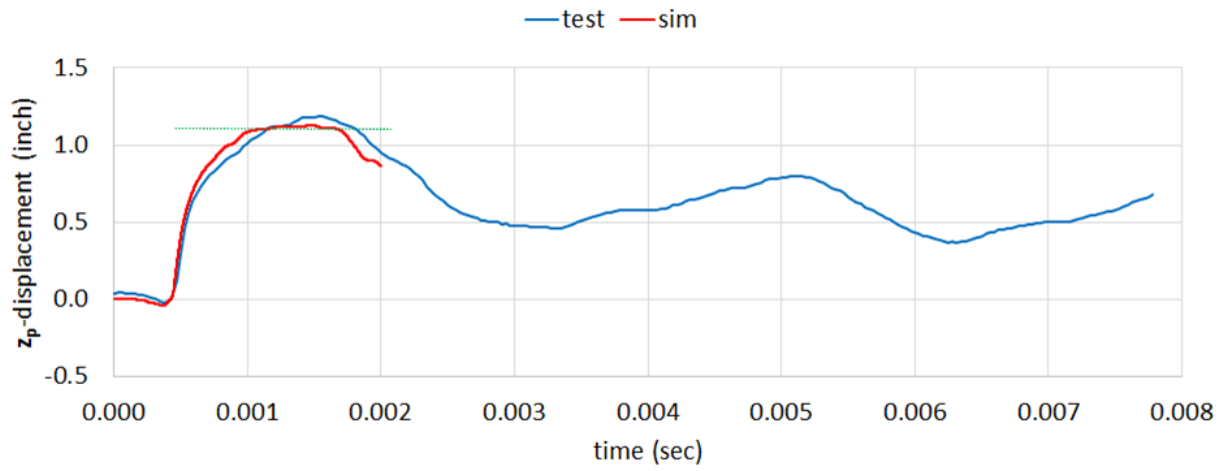

(a)

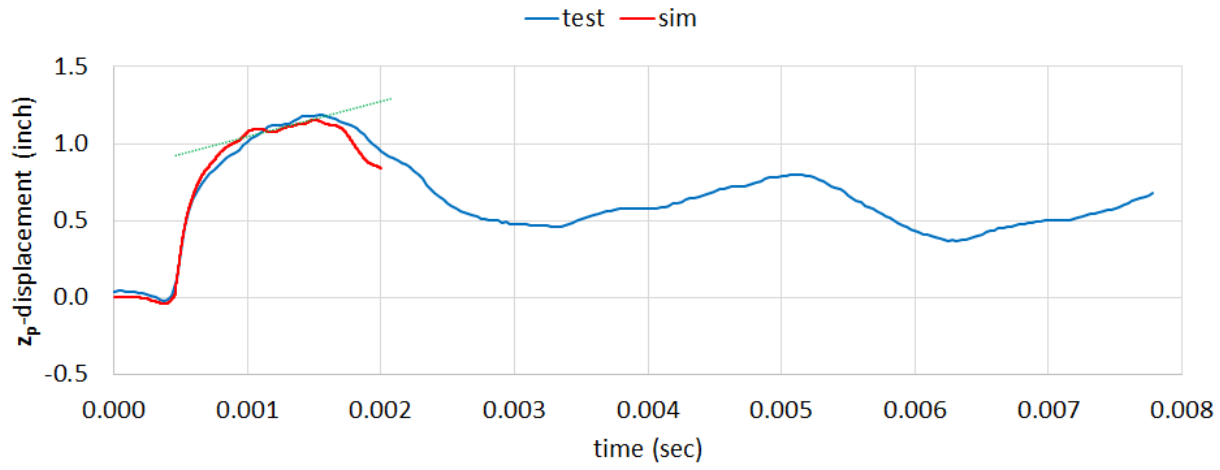

(b)

Figure 25. Comparison of the displacement time histories of the maximum displacement point on the back surface of the panel in LG908: (a) simulation with the half-symmetric FE model and (b) simulation with the full FE model

4.2 LG909

Figure 26(a) shows the blade projectile position at the moment of impact in test LG909. The initial setups of the ballistic simulations of LG909 using the half-symmetric and full FE models are shown in Figure 26(b) and Figure 26(c), respectively. The **X**-velocity of the projectile is 813.2 ft/s, which is the highest in all four tests and about 100 ft/s higher than in LG908.

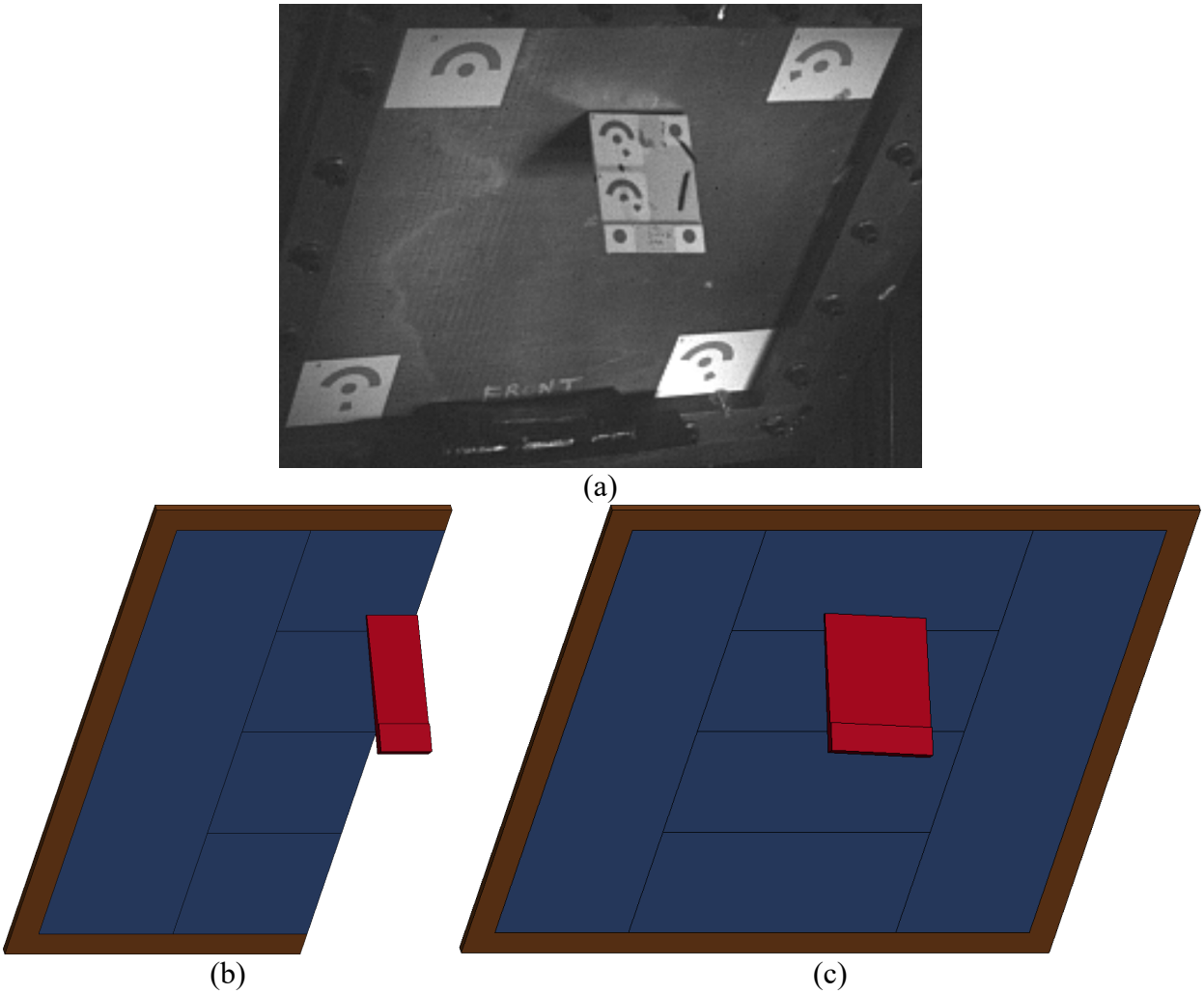

(a)

(b) (c)

Figure 26. The blade projectile posture at the impact moment of the LG909: (a) test, (b) simulation using the half-symmetric FE model, and (c) simulation using the full FE model

Figure 27(a) shows the panel deformation in the LG909 test. It can be seen that the panel surface was worn initially by the blade root edge and then eventually perforated. During the wear process, much debris was ejected. After that, the cracks propagated downward and the large petal developed with a big opening in the panel. However, the blade projectile did not fully penetrate the panel.

Figure 27(b) and Figure 27(c) show the panel deformations of LG909 simulations in an effective plastic strain contour using the half-symmetric and full models, respectively. The wear mark, perforation and petal on the panel were similar to the test. However, the lengths of the wear mark and cracks are shorter than in the test, which is probably due excessive erosion of solid elements in the wear area, and the necessary use of contact friction coefficients in the simulations rather than a representation of the actual tribochemical friction process. Comparing the simulations, the wear mark, perforation and petaling are close, except for the left crack propagation direction. The left crack was initially propagating to the left and then turned downward due to the roll and yaw motions of the blade projectile in the simulation with the full FE model.

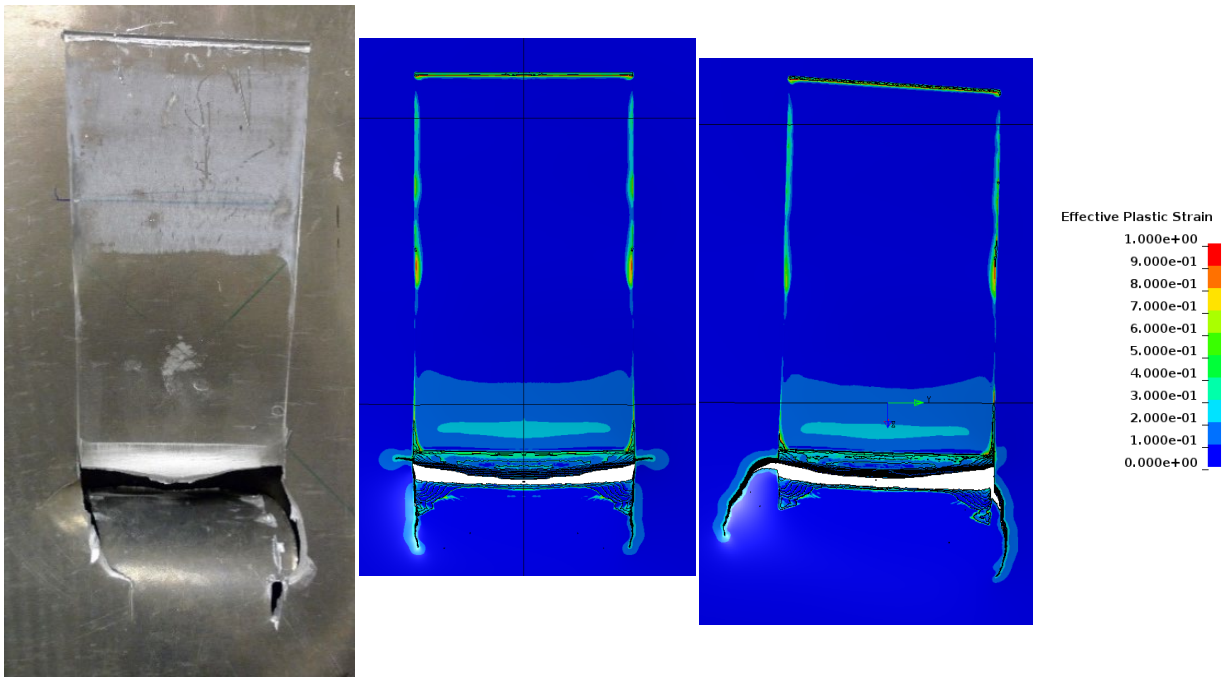

(a) (b) (c)

Figure 27. Panel deformation in LG909: (a) test (b) simulation at 2 msec using the half-symmetric FE model, and (c) simulation at 2 msec using the full FE model

Figure 28 shows the energy balance plots of the simulations of LG909. It can be confirmed that the hourglass energy and contact energy (obtained by subtracting the friction energy from the sliding interface energy) are very small. The eroded internal energy takes about 13% of the internal energy, which is about 5% smaller than in the simulations of LG908. Because the wear area is larger in LG908 than in LG909, the eroded internal energy in LG909 is smaller than in LG908.

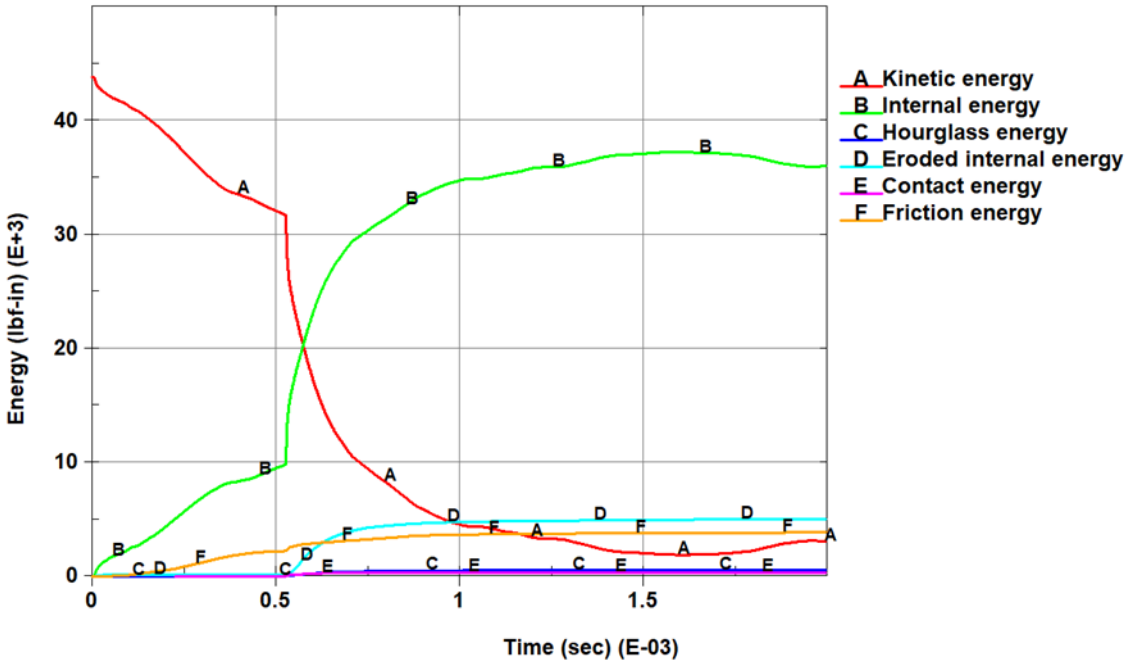

(a)

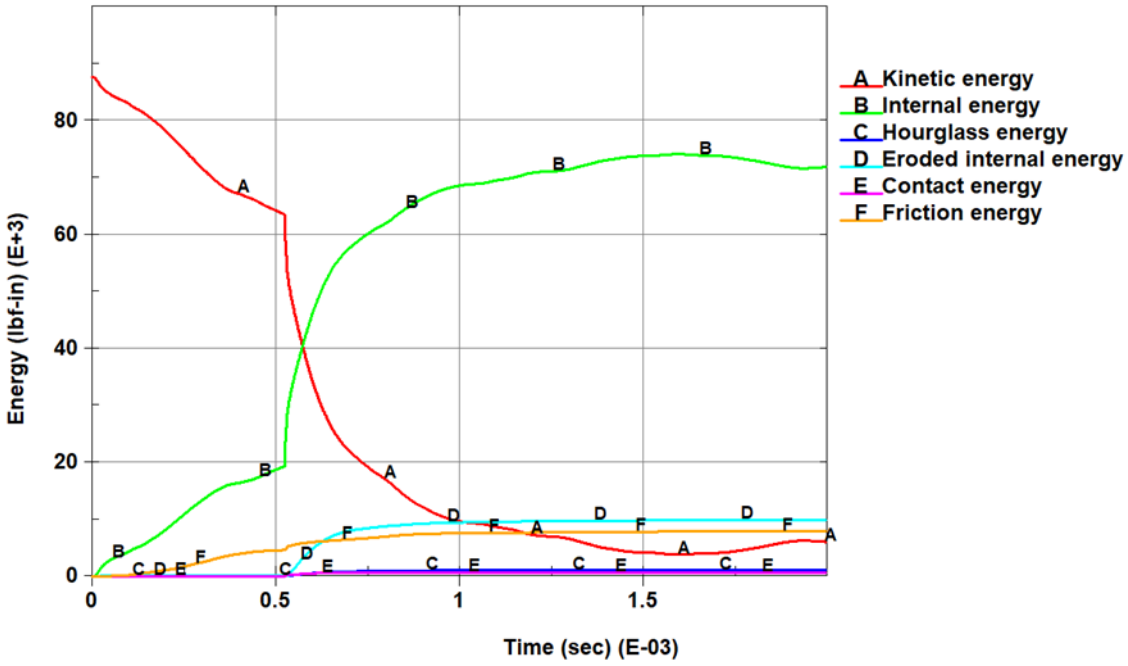

(b)

Figure 28. Energy balance plots of the simulations of LG909: (a) the half-symmetric FE model and (b) the full FE model

Table 5 describes the three stages of the impact process of the blade projectile on the panel: the first stage is at the time right before the root of the blade projectile impacted the panel; the

second stage is at the time right before a crack was initiated in the test; the third stage is at the time when the panel deformation reached the maximum. The timing of each stage is very close between test and the simulations, except the maximum displacement time in Stage3.

Table 5. Three stages of the impact process of the blade projectile on the panel in LG909

LG909	**Test**	**Simulation**		**Note**
		Half-symmetric FE model	**Full FE model**	
Stage1	0.53 msec	0.53 msec	0.54 msec	Root impact
Stage2	0.62 msec	0.62 msec	0.62 msec	Crack initiation
Stage3	1.63 msec	1.48 msec	1.43 msec	Max displacement

Figure 29 shows the comparison of the deformation profiles of the central vertical cross-section of the panel between the test and simulation at each stage of LG909. In Stage1, they are almost identical. In Stage2, the deformation profile of the simulation with the half-symmetric FE model is very close to the one in the test, but the deformation profile of the simulation with the full FE model is a little lower than the one in the test, which was probably due to a 0.01 msec time delay in Stage1.

In Stage3, the deformation curves are discontinuous due to failure in the middle. The deformation profiles between the test and both simulations are very close up to the time when crack initiation occurred. Following crack initiation, however, the deformation in the test is much larger than in the simulations. The final deformed shape of the petal is directly related to the length of the crack. Note that the test crack length in Figure 27(a) is noticeably longer than the simulation crack lengths in Figure 27(b) and Figure 27(c). Crack propagation, final crack lengths and petal deformations are inherently highly varied. Crack propagation requires much less energy than the initial crack formation. As a result, crack length and petal deformation are dependent on small differences in energy. They also depend on microstructures such as grain boundaries in the metal. Crack propagation models exist; however, no attempt to incorporate them into this research has been made. Crack propagation models have not been incorporated into *MAT_224. Figure 30 compares the displacement contours of the panel at the maximum displacement time in LG909 between the test and simulation with the half-symmetric FE model. It shows that the overall deformation of the panel compares well even though the petal in the simulation was not developed as much as in the test.

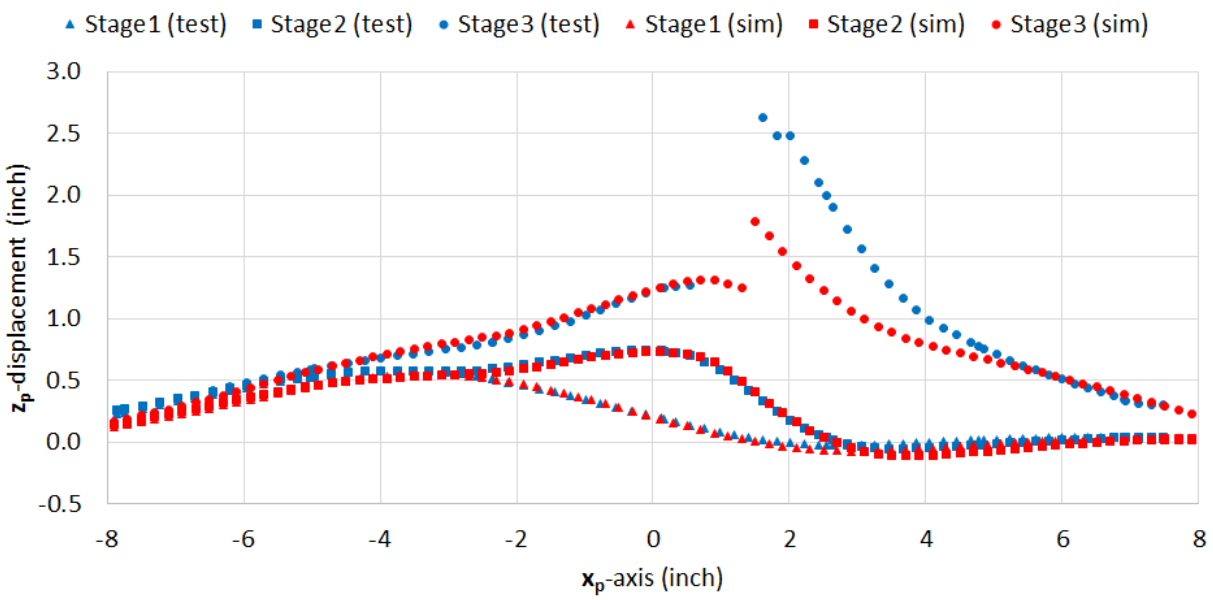

(a)

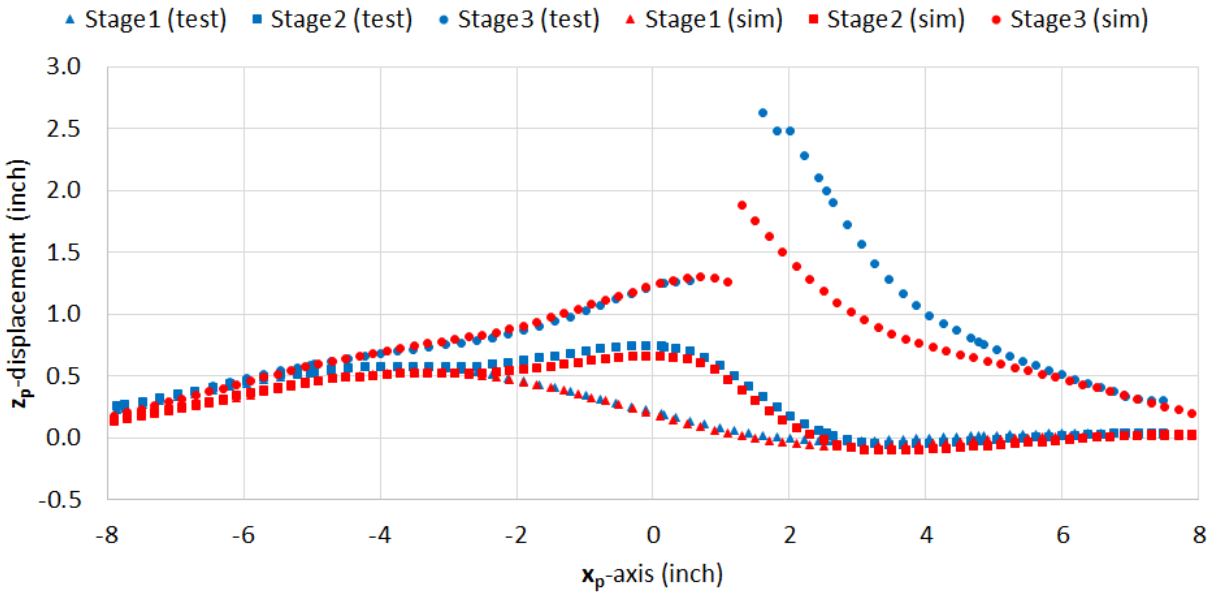

(b)

Figure 29. Comparison of deformation profiles of the central vertical cross-section of the panel in LG909: (a) simulation with the half-symmetric FE model and (b) simulation with the full FE model

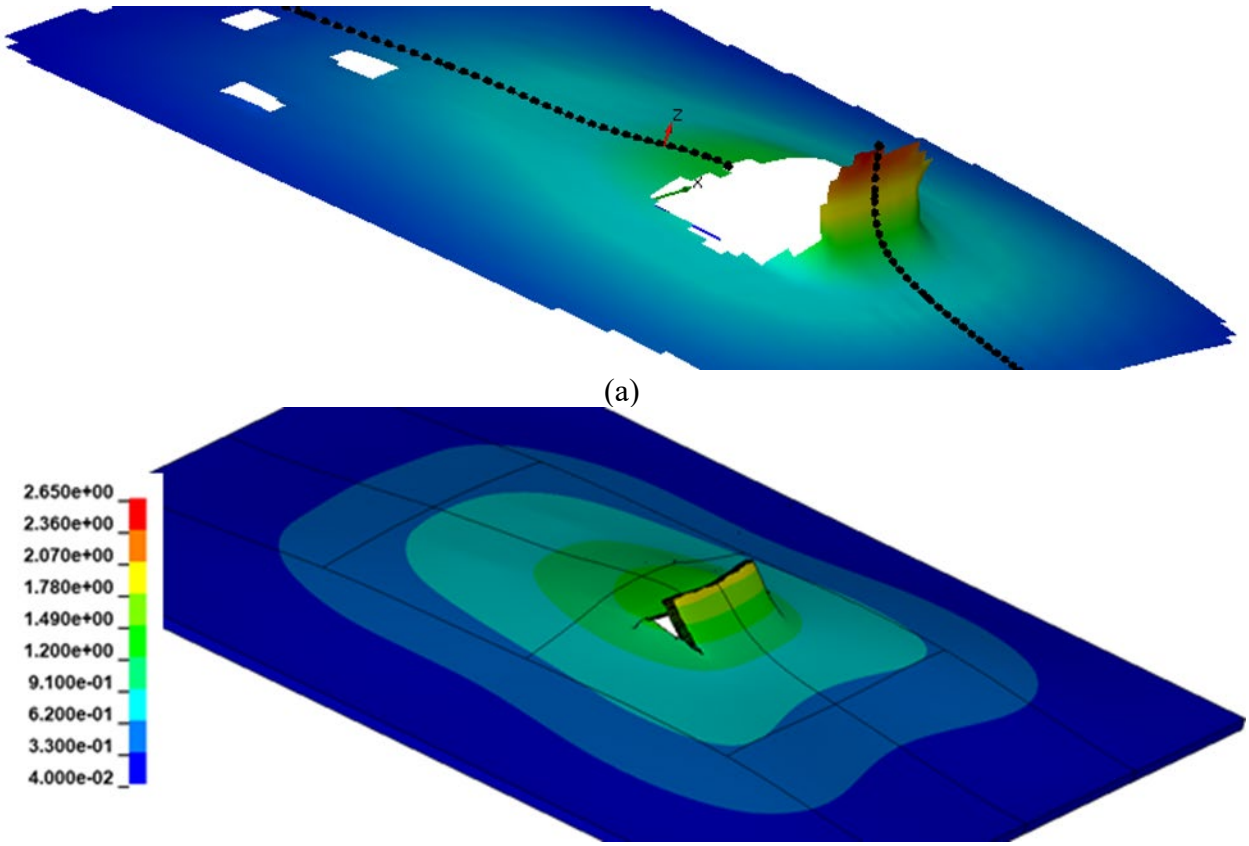

Figure 30. Displacement contour of the panel at the maximum displacement time in LG909 (units in inches); (a) test, and (b) simulation with the half-symmetric FE model

4.3 LG910

The blade projectile position at the moment of impact in the LG910 test is shown in Figure 31(a), and the initial setups of the ballistic simulations of LG910 using the half-symmetric and full FE models are shown in Figure 31(b) and Figure 31(c), respectively. The **X**-velocity of the projectile is 760.7 ft/s, which is about 50 ft/s lower than the one in LG909 and also about 50 ft/s higher than the one in LG908.

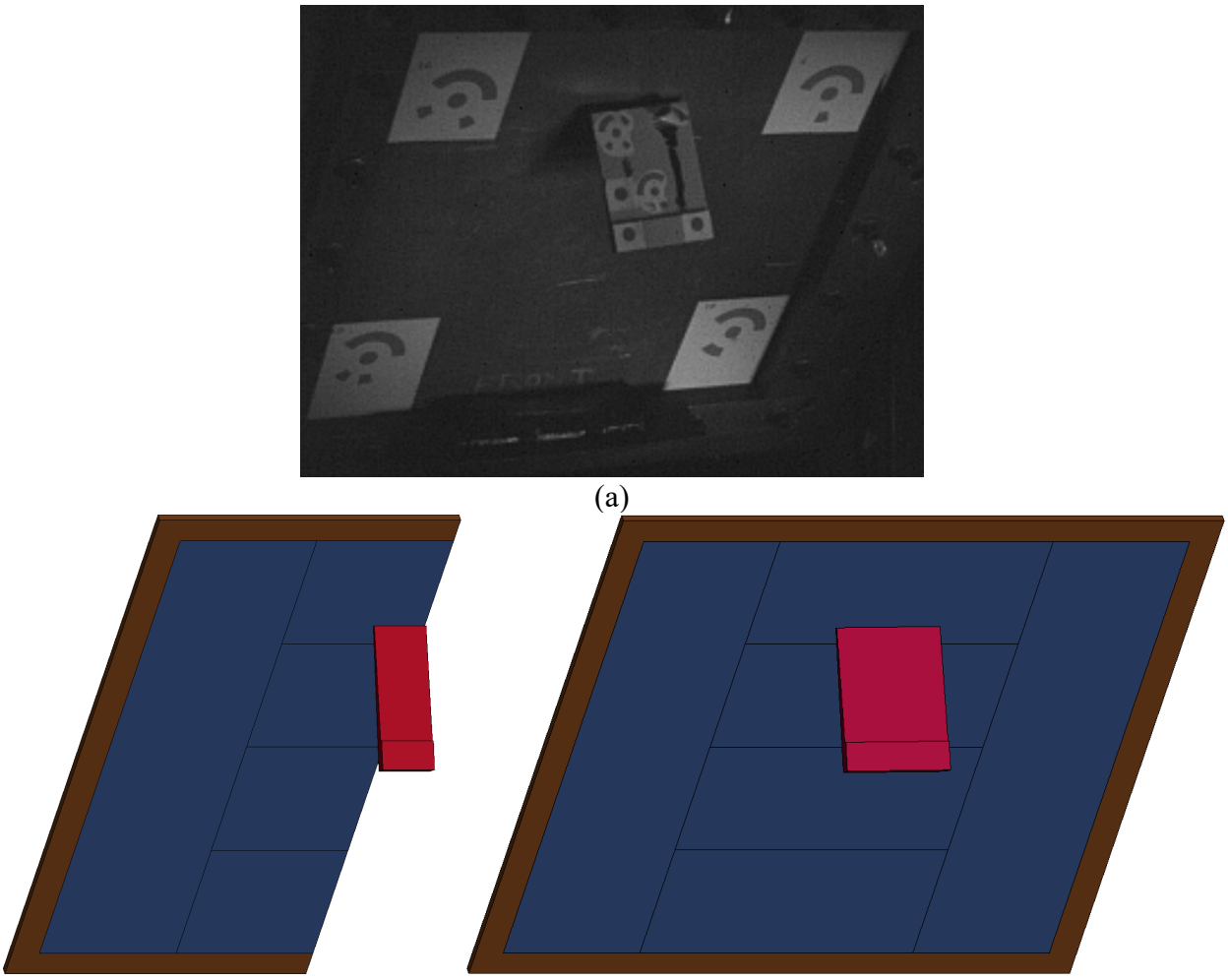

(a) (b) (c)

Figure 31. The blade projectile posture at the impact moment of the LG910: (a) test, (b) simulation using the half-symmetric FE model, and (c) simulation using the full FE model

Figure 32(a) shows the panel deformation in the LG911 test. The panel was perforated, but the blade projectile did not penetrate the panel completely. The panel deformation in LG910 is very similar to that in LG909. The petal size and deformation in LG910 are smaller than in LG909 due to the lower **X**-velocity of the blade projectile.

Figure 32(b) and Figure 32(c) show the panel deformations of the LG910 simulations in an effective plastic strain contour using the half-symmetric and full models, respectively. Similar to the simulations of LG909, the lengths of the wear mark and cracks are shorter than those in the test. The simulation results are similar, except for the crack propagation direction. In the half-symmetric model simulation, both the left and right cracks initially propagated slightly toward the side and then turned downward, but in the full FE model simulation both cracks propagated directly downward.

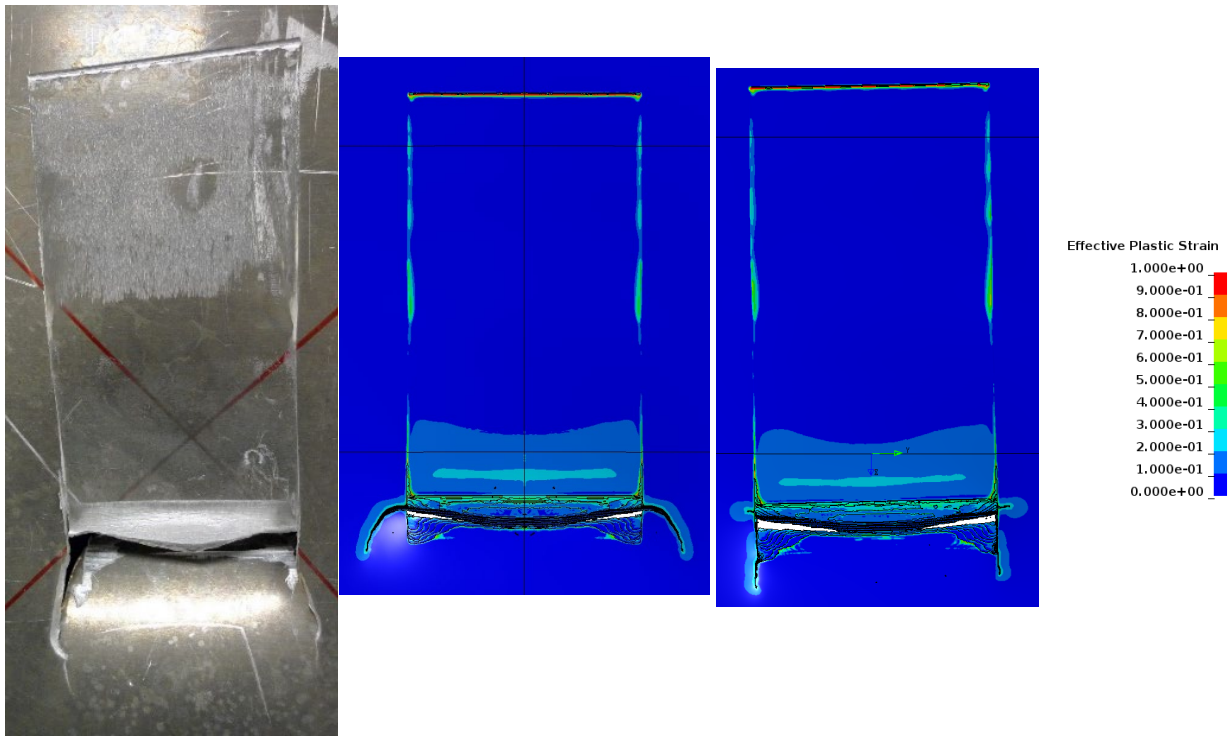

(a) (b) (c)

Figure 32. Panel deformation in LG910: (a) test (b) simulation at 2 msec using the half-symmetric FE model, and (c) simulation at 2 msec using the full FE model

4.4 LG911

The blade projectile position at the moment of impact in the LG911 test is shown in Figure 33(a), and the initial setups of the ballistic simulations of LG911 using the half-symmetric and full FE models are shown in Figure 33(b) and Figure 33(c), respectively. The **X**-velocity of the projectile is 723.3 ft/s, which is just about 10 ft/s higher than in LG908.

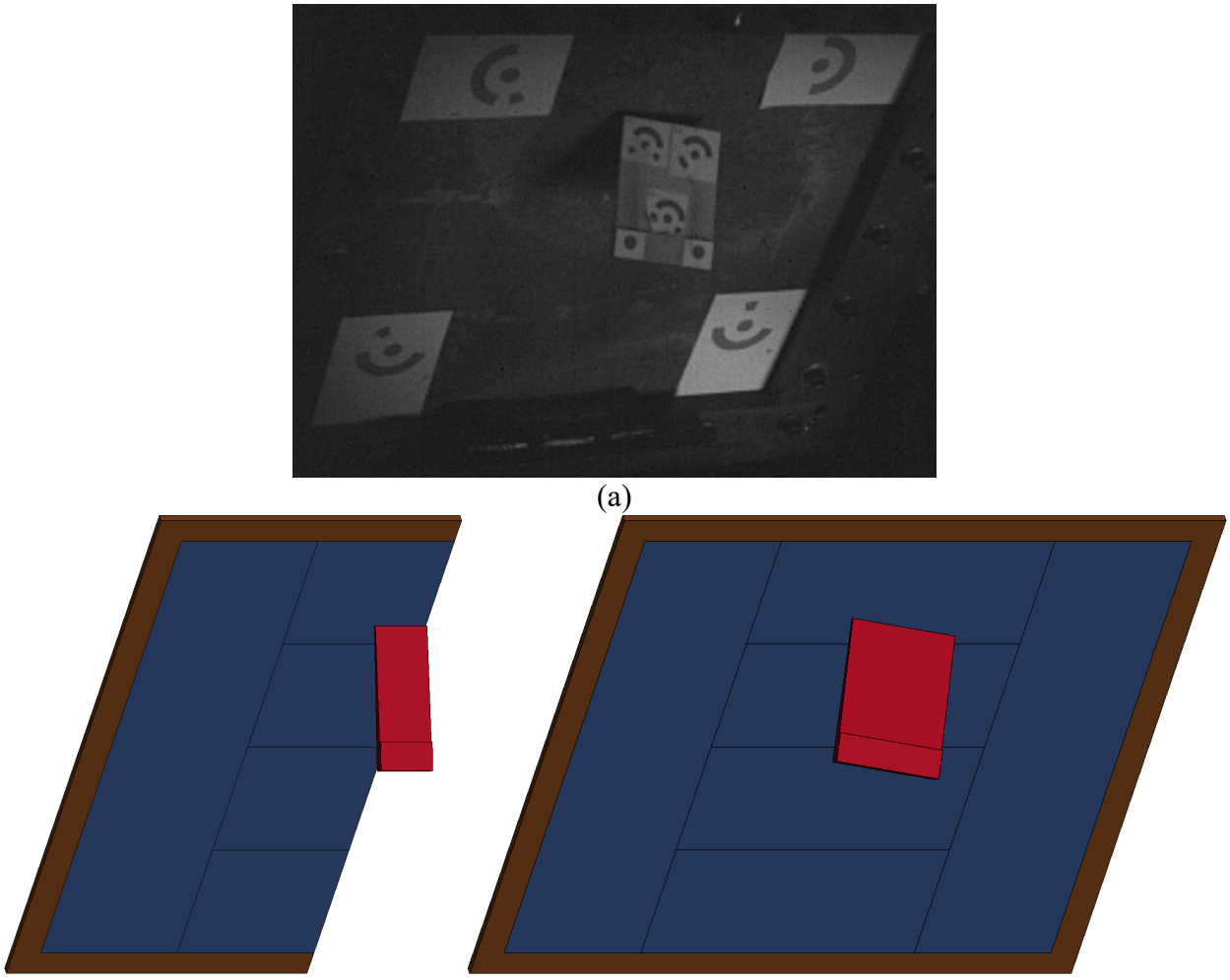

(a) (b) (c)

Figure 33. The blade projectile posture at the impact moment of the LG911: (a) test, (b) simulation using the half-symmetric FE model, and (c) simulation using the full FE model

Figure 34(a) shows the panel deformation in the LG911 test. The panel was perforated, but the blade projectile did not penetrate the panel thoroughly. The panel deformation in LG911 is very similar to the deformations in LG909 and LG910.

Figure 34(b) and Figure 34(c) show the panel deformations for the LG911 simulations in an effective plastic strain contour using the half-symmetric and full FE models, respectively. The deformation in the simulation with the half-symmetric FE model shows small perforations at both sides of the wear mark, and those perforations did not propagate to make a wide opening and petal on the panel. In the simulations with the full FE model, the perforation initiated at the right side of the wear area and propagated to the left, but not enough to reach to the left side edge of the wear area to make a complete opening on the panel.

The deformations of the panel between test and simulations are quite different in LG911. Based on the test results, it was found that the **X**-velocity of the projectile in LG911 is close to the critical velocity for panel perforation. For that reason, the panel deformation in LG911 could be very sensitive to small variations in the 3D movements of the blade projectile in the test. If the 3D position and velocity of the projectile at the moment of impact are not precisely identified in the post-test calculations, or not accurately implemented in the simulation model, then there may be significant differences between the simulation and test. In addition, this difference is significantly influenced by crack propagation mechanics in the test, and the lack thereof in the analysis as presented in Section 4.2. Nevertheless, the simulations were able to predict the initiation of the perforation in the panel with the measured impact velocity of the projectile.

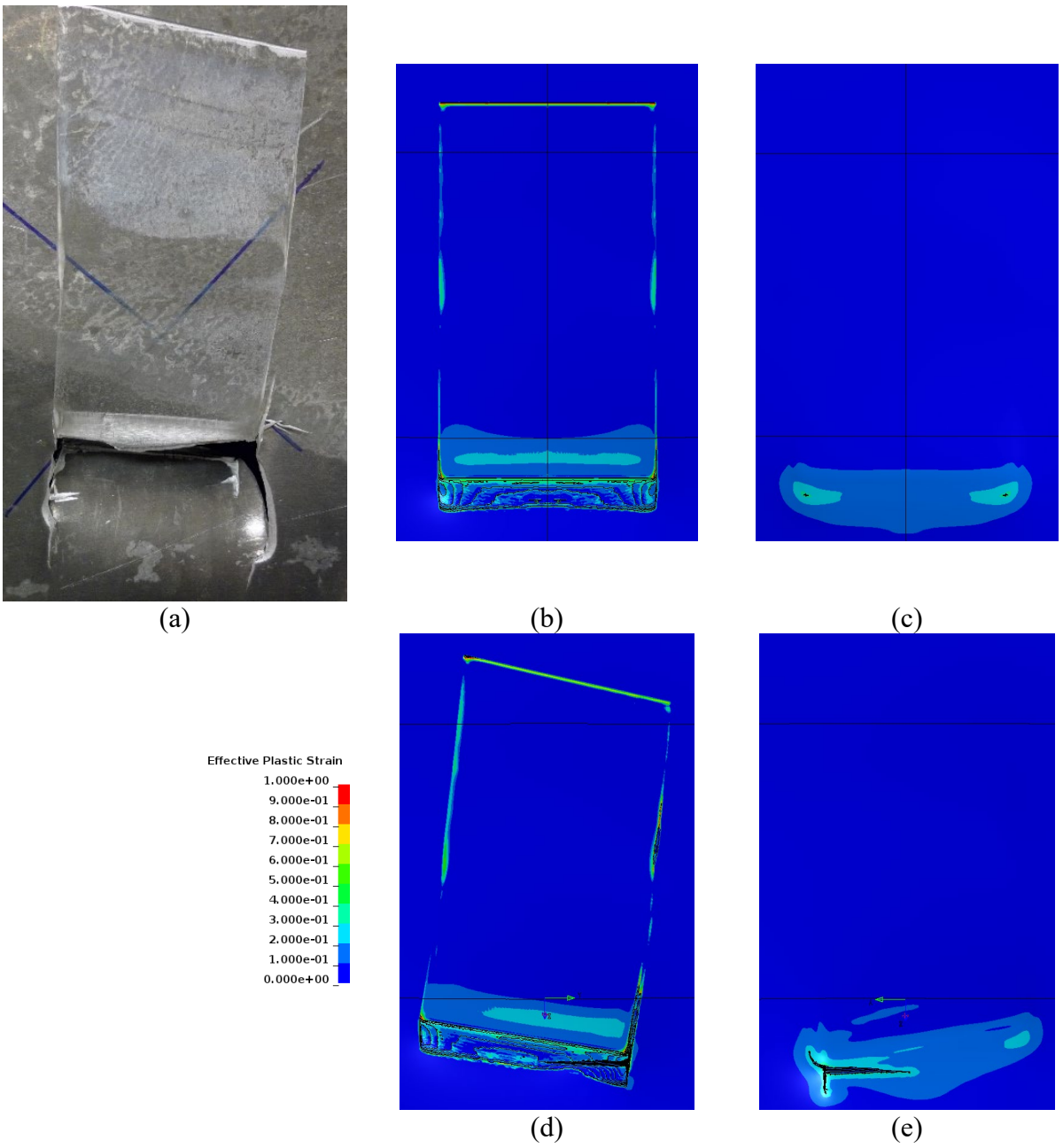

Figure 34. Panel deformation in LG911: (a) test (b) front view at 2 msec in the simulation using the half-symmetric FE model, (c) rear view at 2 msec in the simulation using the half-symmetric FE model, (d) front view at 2 msec in the simulation using the full FE model, and (e) rear view at 2 msec in the simulation using the full FE model

4.5 Summary

The half-symmetric and full FE model simulations showed very similar results to the tests in terms of panel deformation and blade behavior, with the exception of test LG911. The initial setup of the simulation models closely replicated the behavior of the blade projectiles in test and caused similar panel deformations by creating wear marks and perforation on the panel. However, the panel crack and petal characteristics in the simulation of LG911 were not fully developed, unlike what was observed in test. It is important to note that the **X**-velocity of the blade projectile in LG911 is close to the critical velocity for initiation of panel perforation, so the panel deformation could be very sensitive to small variations of the 3D movements of the blade projectile in that test. In addition, the difference could be also caused by the inherent limitations of the simulation: such as the use of element erosion to represent rupture, the use of friction coefficients to represent tribochemical physics, and the non-inclusion of crack propagation mechanics.

The generic difference between the tests and simulations stemmed from the wear process between the panel and blade projectile, such as the presence of expelled wear debris and the size and length of wear marks on the panel. In all simulations, solid elements in the wear area were eroded, while in the test significant quantities of wear debris fell away. It is unclear if the eroded internal energy in the simulation is larger than or equivalent to the absorbed energy to create the wear debris in the test. Physically however, friction coefficients in conjunction with mechanical wear, and tribochemical wear, are different phenomena and this difference affects the simulation results relative to the test. The static and dynamic contact friction coefficients were set to 0.3 in all simulations for both the half-symmetric and full FE models, and they worked well to create the perforation in the panel in LG909, LG910 and LG911. However, if the level of friction is not selected carefully, it could adversely affect the wear mark size, crack propagation, and petal size in the simulations. As previously presented, a constant fiction coefficient does not represent that physical dependency on rate, pressure, and mesh size.

The simulations using the half-symmetric and full FE models were compared against one another to see the effects of roll and yaw motions for the blade projectile. Overall, they gave similar simulation results. However, the roll and yaw motions of the blade projectile affected the crack propagation pattern leading to development of the petal opening in the panel. The effects of projectile attitude angle variation were studied in previous research (Park, et al., 2020), which demonstrated that the attitude angle variation of the projectile could affect the crack propagation pattern sensitivity. Nevertheless, it appears that for this test series, the range of blade projectile variation in roll and yaw motions is small enough that it is not expected to have significant

influence on the overall panel deformation and perforation in the simulations of the half-symmetric and full FE models.

5 Conclusions

In this research work, four ballistic blade impact tests were simulated using advanced Aluminum 2024 and Titanium 6Al-4V material models utilizing *MAT_224 in LS-DYNA. These simulations were performed to validate these material models under more realistic turbine engine blade release event conditions than previously modeled ballistic impact tests.

The half-symmetric and full FE models were developed with 41 million and 82 million solid elements with a 0.01-inch element size, respectively. The initial condition, contact parameters, contact friction, and boundary conditions of the FE models were studied to implement the 3D movements and rotations of the blade projectile accurately in the simulations.

The four ballistic impact simulations showed similar results to the tests in terms of the panel deformation and blade behavior, and were able to predict the panel perforation. The initial stages of the simulation model impact closely replicated the behavior of the blade projectile and caused similar panel deformation by creating wear marks and perforation on the panel. However, the crack and petal in the panel in the simulation of LG911, where the **X**-velocity of the blade projectile is near the critical velocity of the panel perforation, were not fully developed, unlike in the test. It is noteworthy that the ballistic impact simulations using the *MAT_224 metallic material models demonstrate the ability to predict the onset of perforation.

The fundamental difference between the tests and simulations was from the wear process of the panel by the blade projectile, including the presence of the wear debris and the size of the wear mark on the panel. The generic limitation of the simulation, such as constant friction coefficients and mechanical element erosion, which resulted in the absence of wear debris, probably affected the wear mark size, crack propagation, and petal size in the simulations.

Comparing the two simulations using the half-symmetric and full FE models, the small variation of the roll and yaw movements of the blade projectile was not very influential to the overall panel deformation and perforation in the simulations. However, these variations affected the crack propagation pattern to develop the petal and opening in the panel.

6 References

Buyuk, M. (2014). *Development of a New Metal Material Model in LS-DYNA, Part 2: Development of a Tabulated Thermo-Viscoplastic Material Model with Regularized Failure for Dynamic Ductile Failure Prediction of Structures under Impact Loading.* Final Report, Federal Aviation Administration, U.S. Department of Transportation. Retrieved from http://actlibrary.tc.faa.gov

Dong, H., & Bell, T. (1999). Tribological Behaviour of Alumina Sliding against Ti6Al4V in Unlubricated Contact. *Wear*, 874-884.

Emmerling, W., Altobelli, D., Carney, K., & Pereira, M. (2014). *Development of a New Metal Material Model in LS-DYNA, Part 1: FAA, NASA, and Industry Collaboration Background.* Technical Report, Federal Aviation Administration, U.S. Department of Transportation. Retrieved from http://actlibrary.tc.faa.gov

Haight, S., Wang, L., Du Bois, P., Carney, K., & Kan, C. D. (2016). *Development of a Titanium Alloy Ti-6Al-4V Material Model Used in LS-DYNA.* Final Report, Federal Aviation Administration, U.S. Department of Transportation. Retrieved from http://actlibrary.tc.faa.gov

Hammer, J. T. (2014). *Plastic Deformation and Ductile Fracture of Ti-6Al-4V under Various Loading Conditions.* Technical Thesis, Federal Aviation Administration, U.S. Department of Transportation. Retrieved from http://actlibrary.tc.faa.gov

Kelley, S., & Johnson, G. (2006). *Statistical Testing of Aircraft Materials for Transport Airplane Rotor Burst Fragment Shielding.* Final Report, Federal Aviation Administration, U.S. Department of Transportation. Retrieved from http://actlibrary.tc.faa.gov

LS-DYNA Aerospace Working Group. (2021). Retrieved from https://awg.lstc.com/tiki-index.php?page=Material+Parameter+Sets

LSTC. (2017). *LS-DYNA Keyword User's Manual, Volume I and II, Version R10.0.* Livermore, California: Livermore Software Technology Corporation.

Mishra, A. (2014). Analysis of Friction and Wear of Titanium Alloys. *International Journal of Mechanical Engineering and Roborics Research, 3*(3), 570-573.

Park, C. K., Carney, K., Du Bois, P., Cordasco, D., & Kan, C. D. (2020). *Aluminum 2024-T351 Input Parameters for *MAT_224 in LS-DYNA.* Final Report, Federal Aviation

Adminstration, U.S. Department of Transportation. Retrieved from http://actlibrary.tc.faa.gov

Park, C. K., Queitzsch, G., Carney, K., Du Bois, P., Kan, C. D., Cordasco, D., & Emmerling, W. (2020). *Aluminum 2024-T351 Input Parameters for *MAT_224 in LS-DYNA, Part 3: Ballistic Impact Simulations of an Aluminum 2024 Panel Using *MAT_224 in LS-DYNA Considering Oblique Incidence and Attitude Angles of a Rectangular Projectile.* Final Report, Federal Aviation Administration, U.S. Department of Transportation. Retrieved from http://actlibrary.tc.faa.gov

Pereira, M., Revilock, D., Lerch, B., & Ruggeri, C. (2013). *Impact Testing of Aluminum 2024 and Titanium 6Al-4V for Material Model Development.* Technical Memorandum, National Aeronautics and Space Administration. Retrieved from https://ntrs.nasa.gov/citations/20130013684

Seidt, J. D. (2014). *Development of a New Metal Material Model in LS-DYNA, Part 3: Plastic Deformation and Ductile Fracture of 2024 Aluminum under Various Loading Conditions.* Final Report, Federal Aviation Administration, U.S. Department of Transportation. Retrieved from http://actlibrary.tc.faa.gov